Unsteady hydrodynamic forces of solid objects vertically entering the water surface

J. Wang[1,2], O. M. Faltinsen[2] and C. Lugni[2,3]

[1]*College of Shipbuilding Engineering, Harbin Engineering University, Harbin, China*

[2]*Centre for Autonomous Marine Operations and Systems (AMOS), Norwegian University of Science and Technology, N-7491 Trondheim, Norway*

[3]*CNR-INSEAN: Italian Research Council – Institute for Marine Technology, Roma, Italy*

We investigate the unsteady hydrodynamic force of solid objects vertically entering water with an air cavity behind the falling body. Physical models are proposed to represent the force components corresponding to the body acceleration, the gravity and the velocity of the body and the fluid particles. The theoretical or numerical solutions of the physical models are presented to understand the evolution of the force components. The body-acceleration force component is expressed as the high-frequency added mass times the body acceleration. Near the undisturbed free surface, the added mass grows strongly with increasing the submerged depth. It tends to be steady after the submerged depth is greater than a few characteristic lengths. The gravity force component consists of an upward hydrostatic term and a downward dynamic term. Generally, the hydrostatic term, which is obtained by integrating the gravity term in the Bernoulli's equation over the wetted body surface, is much larger than the gravity force component. For the three-dimensional bodies, the gravity force component is found to vary as a power of the submerged depth, where the exponent is about 0.83. The velocity force component is represented as the drag coefficient defined by the V-squared law, which is characterized by the body geometry. The drag coefficient may experience three successive stages with increasing the submerged depth.

I. INTRODUCTION

Solid objects entering a water (liquid) surface often involves large unsteady hydrodynamic loads and rapid deformation of free surface. The phenomena are of great interest to the study of seaplane landing,[1] ship slamming,[2] planning vessels,[3] air-to-sea projectiles,[4-7] and the impacting of waves on solid structures.[8-9] Even the relevant hydrodynamics play an important role in biological creatures walking on water.[10-11] The initial stage of water entry, characterized by the jet flow on the body surface, has been widely studied.[12-23] During this period, the hydrodynamic force on the body is dominated by the change rate of momentum of the added fluid mass, which can be related to the change rate of area of the wetted body surface.[1, 2, 24] If the water-entry speed is sufficiently large, an air cavity will be formed behind the falling body.[7] The cavity expands at the beginning and the gravity effect resists the expansion of the cavity causing its contraction and pinch-off (closure).[25] This stage involves two important aspects: (i) the evolution of the air cavity behind the falling body; and (ii) the hydrodynamic force on the body. The cavity dynamics of solid objects vertically entering the water surface have been extensively investigated,[4-6, 11, 24-32] since Worthington & Cole's work[26]. The hydrodynamic force on the body is essentially transient and it plays key role in modeling the projectile dynamics. Very few literatures can be found on the deep investigation of the transient hydrodynamic force, which is the focus of the present work.

Plesset & Shaffer studied the drag force of the steady cavity flow past symmetrical wedges.[33] A cavitation number of zero results in an infinite cavity, which corresponds to the limiting state of a wedge vertically entering the water surface with constant speed in a gravity-free environment. It was reported that the predicted drag coefficients of zero cavitation number agree well with experimental data.[34] May & Woodhull investigated the drag coefficients of steel spheres entering water vertically.[35] The drag coefficient was defined by the relation $C_D = \text{drag}/(0.5\rho V^2 \pi R^2)$, where ρ is the density of the water, V is the velocity of the sphere, and R is the radius of the sphere. For the evaluation of the drag coefficient defined by the V-squared law, they suggested excluding all forces having a different independence on V. Then the equation of motion of the body was expressed as

$$M\frac{dV}{dt} = Mg - C_D\frac{1}{2}\rho V^2\pi R^2 - \rho ghS + (p_c - p_a)S, \tag{1}$$

where M is the mass of the sphere, g is the acceleration of gravity, h is the submerged depth of the sphere, S is the projected wetted area, p_c is the cavity pressure and p_a is the atmospheric pressure. Their analysis used $S = 0.45\pi R^2$ instead of the measured value $0.8\pi R^2$ for the evaluation of the term, ρghS, giving satisfactory results. It implies that the force obtained by directly integrating the hydrostatic term in the Bernoulli's equation over the wetted body surface strongly overestimates the force due to the gravity effect, which is confirmed by Yan $et\ al.$[31]. The reason for this will be explained by the present work and the proper method for the evaluation of the force due to the gravity effect will be proposed. The force due to the body acceleration, i.e. the added mass force, was neglected. It is safe because in their study the mass ratio defined by $D = M/A_{33}$ (A_{33} is the vertical added mass of the sphere and is estimated as $\rho\pi R^3/3$) is as large as about 31 and the Froude number, $Fn = V/\sqrt{gR}$, is sufficiently high. The added mass force should appear as an independent term at relatively small mass ratios and Froude numbers.[32] Furthermore, the last term in Eq. (1) is due to the air flow and can be neglected at relatively small entry velocities.[32, 36-37]

In this work, the unsteady hydrodynamic force of solid objects vertically entering water with an air cavity behind the falling body is deeply investigated within the framework of potential flow. By neglecting the surface tension and the air flow, the hydrodynamic force is decomposed into the components corresponding to the following physics: i) the body acceleration; ii) the gravity; and iii) the velocity of the body and the fluid particles. Exact physical models are proposed to represent the force components. The physical models for the force components dependent on the body acceleration and the gravity are simplified by assuming a uniform air cavity, which gives good results. The numerical/analytical solutions of the physical models are presented for understanding the evolution of the force components. The key physical parameters of affecting the force components are explored and discussed in details.

II. DECOMPOSITION OF UNSTEADY FORCE

Consider a solid object with mass M and breadth $2c_0$ vertically impacting the still water surface with initial entry speed V_0. The surface tension σ can be neglected provided that the Weber number $W = \rho V_0^2 c_0/\sigma \gg 1$. Viscous effects may be excluded within the short duration of the impact and for high Reynolds number $Re = \rho V_0 c_0/\mu$. Further, we neglect the influence of the air flow. Then the impact is characterized by the body geometry, the Froude number $Fn = V_0/\sqrt{gc_0}$, and the mass ratio $D = M/A_{33}$. Here, the vertical added mass A_{33} of the body can be estimated as $0.5\rho\pi c_0^2$ for two-dimensional cases and $4\rho c_0^3/3$ for three-dimensional cases.
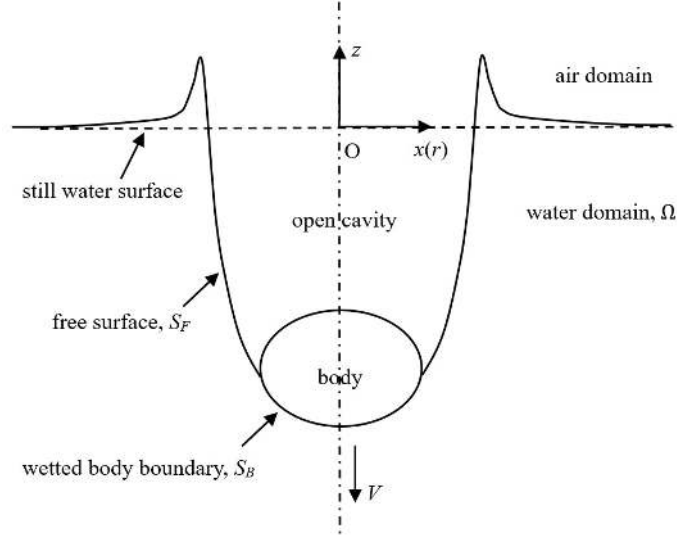
Fig. 1. Sketch of a symmetrical body vertically entering the water surface. V denotes the instantaneous speed of the body.

Fig. 1 illustrates a symmetrical body vertically entering the water surface with an open cavity behind the falling body. Ω denotes the water domain, S_F the free-surface boundary and S_B the wetted body boundary. In the two-dimensional space, a Cartesian coordinate system is adopted: the x-axis is along the horizontal direction and coincides with the still water surface; the z-axis is along the vertical direction in the center plane of the body and is positive upwards. In the three-dimensional space, a cylindrical coordinate system is adopted: the radial axis, r-axis, is parallel to the still water surface; the z-axis coincides with the symmetrical axis of the body and is positive upwards. These notations and coordinate systems are used throughout the paper.

Assuming that the flow is irrotational and the water is incompressible, the water flow can be well represented by the potential-flow model.[30, 37] The velocity potential satisfying Laplace's equation

$$\nabla^2 \varphi = 0 \tag{2}$$

is introduced. The local velocity is given by $\mathbf{u} = \nabla\varphi$. On the wetted body surface, S_B, the impermeability boundary condition holds

$$\frac{\partial \varphi}{\partial n} = \mathbf{V} \cdot \mathbf{n}, \tag{3}$$

where $\mathbf{n}$ is the interior normal to the boundary surface. The water velocity far away from the body should vanish

$$\nabla\varphi = 0. \tag{4}$$

On the free surface, S_F, fully nonlinear kinematic and dynamic boundary conditions are satisfied

$$\frac{D\mathbf{X}}{Dt} = \nabla\varphi, \tag{5}$$

$$\frac{D\varphi}{Dt} = \frac{1}{2}|\nabla\varphi|^2 - gz. \tag{6}$$

Here, $\mathbf{X}$ is the position vector of the water particle and the operator, $\frac{D}{Dt} := \frac{\partial}{\partial t} + \nabla\varphi \cdot \nabla$, is the substantial derivative following the water particle on the free surface. Based on the Bernoulli's equation, the vertical force acting on the body is expressed as

$$F_z = \rho \int_{S_B} \left(gz + \frac{\partial \varphi}{\partial t} + \frac{1}{2}|\nabla\varphi|^2 \right) n_z \, ds. \tag{7}$$

The $\partial\varphi/\partial t$ term can be evaluated by solving the boundary value problem for the auxiliary function $\psi = \partial\varphi/\partial t + \mathbf{V} \cdot \nabla\varphi$. It can be proved that the auxiliary function ψ satisfies the Laplace equation[38]

$$\nabla^2\psi = 0. \tag{8}$$

The Bernoulli's equation gives the Dirichlet boundary condition for ψ on the free surface

$$\psi = \mathbf{V} \cdot \nabla\varphi - \frac{1}{2}|\nabla\varphi|^2 - gz. \tag{9}$$

On the body surface, the boundary condition for ψ can be derived as

$$\frac{\partial\psi}{\partial n} = \dot{\mathbf{V}} \cdot \mathbf{n}. \tag{10}$$

Far away from the body, ψ should vanish

$$\psi = 0. \tag{11}$$

The solution of the function ψ can be divided into three parts $\psi = \psi_1 + \psi_2 + \psi_3$. ψ_1 corresponds to the body acceleration and satisfies

$$\nabla^2\psi_1 = 0 \text{ in } \Omega, \tag{12.a}$$
$$\psi_1 = 0 \text{ on } S_F, \tag{12.b}$$
$$\frac{\partial\psi_1}{\partial n} = \dot{\mathbf{V}} \cdot \mathbf{n} \text{ on } S_B, \tag{12.c}$$
$$\psi_1 \to 0 \text{ at } |\boldsymbol{X}| \to \infty. \tag{12.d}$$

ψ_2 corresponds to the gravity effect and satisfies

$$\nabla^2\psi_2 = 0 \text{ in } \Omega, \tag{13.a}$$
$$\psi_2 = -gz \text{ on } S_F, \tag{13.b}$$
$$\frac{\partial\psi_2}{\partial n} = 0 \text{ on } S_B, \tag{13.c}$$
$$\psi_2 \to 0 \text{ at } |\boldsymbol{X}| \to \infty. \tag{13.d}$$

ψ_3 corresponds to the effect of the velocity of the body and the fluid particles and satisfies

$$\nabla^2\psi_3 = 0 \text{ in } \Omega, \tag{14.a}$$
$$\psi_3 = \mathbf{V} \cdot \nabla\varphi - \frac{1}{2}|\nabla\varphi|^2 \text{ on } S_F, \tag{14.b}$$
$$\frac{\partial\psi_3}{\partial n} = 0 \text{ on } S_B, \tag{14.c}$$
$$\psi_3 \to 0 \text{ at } |\boldsymbol{X}| \to \infty. \tag{14.d}$$

Then the vertical force can be rewritten as

$$F_z = \underbrace{\rho \int_{S_B} \psi_1 n_z \, ds}_{\text{the acceleration term}} + \underbrace{\rho \int_{S_B} (gz + \psi_2) n_z \, ds}_{\text{the gravity term}} + \underbrace{\rho \int_{S_B} (\psi_3 - \mathbf{V} \cdot \nabla\varphi + \frac{1}{2}|\nabla\varphi|^2) n_z \, ds}_{\text{the velocity term}}. \tag{15}$$

The acceleration term, denoted as $F_z^{(a)}$, is proportional to the body acceleration and can be written as $F_z^{(a)} = -A_{33}\dot{V}$, where A_{33} is the high-frequency added mass of the solid object in the vertical direction.

The gravity term, denoted as $F_z^{(g)}$, consists of the 'hydrostatic' term $\rho \int_{S_B} gz n_z \, ds$ and an additional

term $\rho \int_{S_B} \psi_2 n_z \, ds$. The latter is called gravity-induced dynamic term, since the dynamic pressure

component ψ_2 is induced by the gravity. The velocity term, denoted as $F_z^{(v)}$, is related to the body velocity and the velocity field of the water on the deformed free surface and on the body. So far, the unsteady hydrodynamic force has been exactly decomposed into three parts corresponding to different

physics. In the following section, these components of the unsteady force will be analyzed in details.

III. INVESTIGATION OF FORCE COMPONENT

The acceleration term $F_z^{(a)}$, gravity term $F_z^{(g)}$ and velocity term $F_z^{(v)}$ are denoted as the a-term, g-term and v-term force respectively, which are investigated by the numerical and analytical methods.

A. Numerical model

The water-entry problem represented by Eqs. (2)-(6) can be solved by the single-fluid boundary integral method. [37, 40] Here, we outline the key steps of the two-dimensional numerical model and then generalize it for three-dimensional axisymmetric water-entry flows.

Using Green's second identity, the two-dimensional velocity potential can be represented in the boundary integral equation (BIE):

$$\theta \cdot \varphi(x, z) = \int_{\partial\Omega} [\log r \; \mathbf{n} \cdot \nabla\varphi - \varphi \; \mathbf{n} \cdot \nabla \log r] \, ds(\xi, \eta). \tag{16}$$

Here, (x, z) are the field point coordinates, (ξ, η) are the integration coordinates, $r = \sqrt{(\xi - x)^2 + (\eta - z)^2}$, and $\mathbf{n}$ denotes the interior normal to the boundary $\partial\Omega$ of the water domain Ω. In the water, θ is equal to 2π. On $\partial\Omega$, θ is the local interior angle of the boundary. The boundary integral equation is solved by the linear element method: the boundary of the fluid domain is represented by straight line segments; φ and $\partial\varphi/\partial n$ are assumed to vary linearly along each segment; the boundary integral equation is satisfied at the nodal points of segments, which results in the linear equation system for the solution of φ and $\partial\varphi/\partial n$. It notes that other potential functions, such as ψ, can be also solved by the boundary integral method. The body motion and the water flow are solved in a decoupled manner, where the evolution of the free surface is tracked by a second-order Lagrangian method and the motion of the body by a first-order method. The position and velocity potential of the fluid particles on the free surface and the submergence depth, velocity and acceleration of the body, denoted as X_n, φ_n h_n, V_n, $\dot{V}_n$ respectively, are assumed known at time step n. To predict these parameters at step $n+1$, the following time-advancing schemes are adopted: i) solve the velocity potential represented in Eq. (16), based on X_n, φ_n h_n and V_n; ii) evaluate the potential gradient $\nabla\varphi_n$, solve ψ for the vertical force F_z based on $\nabla\varphi_n$ and $\dot{V}_n$, and use F_z to compute $\dot{V}_{n+1}$ by the Newton's second law; iii) transport the body and the fluid particles on the free surface to the intermediate position based on V_n and $\nabla\varphi_n$, resulting in X_*, φ_* and h_* as the first prediction of X_{n+1}, φ_{n+1} and h_{n+1}; iv) solve the velocity potential once more, based on X_*, φ_* h_* and $V_* = V_n + \dot{V}_{n+1}\Delta t$, to obtain $\nabla\varphi_*$; v) finally, we set $X_{n+1} = X_n + \Delta t[\nabla\varphi_n + \nabla\varphi_*]/2$, $\varphi_{n+1} = \varphi_n + \Delta t[(D\varphi/Dt)_n + (D\varphi/Dt)_*]/2$, $h_{n+1} = h_*$ and $V_{n+1} = V_*$. To avoid the fluid particles becoming too close to each other or too far away from each other, the boundary is re-gridded every time step.

The numerical model can be generalized to three-dimensional axisymmetric flows by just changing the boundary integral equation (16) to that for the three-dimensional axisymmetric flows,[39] i.e.

$$\theta \cdot \varphi(r, z) = \int_{\partial\Omega} [\varphi \; \mathbf{n} \cdot \nabla G - G \; \mathbf{n} \cdot \nabla\varphi] \, r \, ds(\xi, \eta). \tag{17}$$

Here, z is the axial coordinate, r is the radial distance, and (ξ, η) are the integration coordinates. The function G is defined as $G = 2K(m)/A$, where $K(m) = \int_0^{\pi/2} \frac{d\theta}{\sqrt{1 - m^2 \sin^2\theta}}$ is the complete elliptic integral of the first kind, $A = \sqrt{(\xi + r)^2 + (\eta - z)^2}$ and $m = 2\sqrt{\xi r}/A$.

At each time step, the force components $F_z^{(a)}$, $F_z^{(g)}$ and $F_z^{(v)}$ can be evaluated through solving Eqs. (12)-(14) by the boundary integral method. Fig. 2 illustrates the evolution of the vertical unsteady force

for the water entry of the wedge corresponding to Wang *et al.* 's experiment.[37] The wedge with a deadrise angle of 30° falls vertically into the calm water with an initial entry speed of 2.5m/s. The half breadth of the wedge is 0.083m and the mass 32.3kg/m. These parameters correspond to $Fn = 2.77$ and the mass ratio of 3. The v-term force is dominant at the beginning and is decreasing with increasing the submerged depth, which is consistent with the deceleration of the wedge. The g-term force increases with the growth of the submerged depth and cannot be neglected when the wedge is deeply submerged. The 'hydrostatic' component strongly overestimates the g-term since the 'dynamic' component results in a significant downward force. The a-term force, i.e. the added mass force, seems negligible compared to the sum of the v-term force and the g-term force. After the closure of the cavity, the air compressibility matters resulting in the oscillation of the hydrodynamic force, which is beyond the scope of this work.
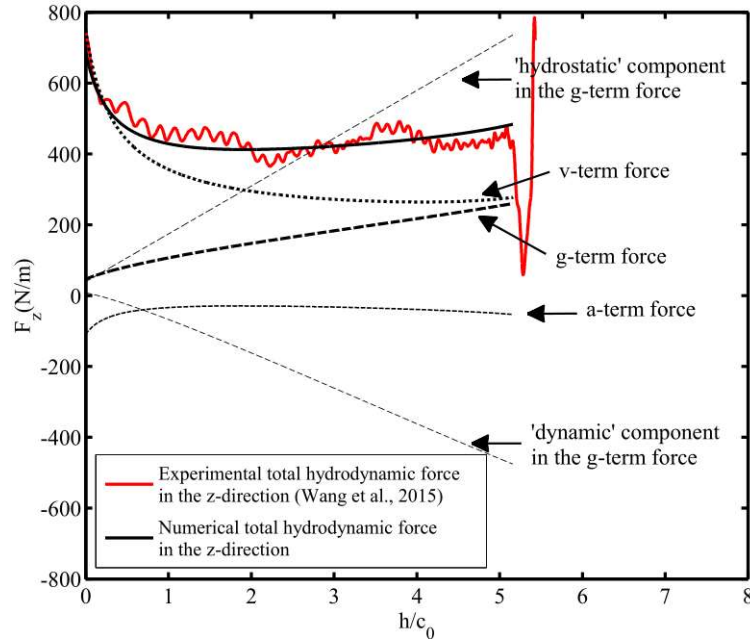
Fig. 2. Evolution of the unsteady force for the vertical water entry of the wedge with deadrise angle 30°, initial entry speed 2.5m/s, half breadth 0.083m and mass 32.3kg/m. The numerical simulation ends at the closure of the cavity; h is the distance between the top of the wedge and the still water surface; c_0 is the half breadth of the wedge. The experimental total hydrodynamic force in the z-direction is computed from the measured body acceleration through the Newton's second law, i.e. $F_z = M(g - \dot{V})$.

Fig. 3 illustrates the evolution of the vertical unsteady force for the water entry of the cone with the same parameters. We note that the mass ratio for the cone is defined by $D = M/(4\rho c_0^3/3)$ and is 3. The evolution of the unsteady force for the cone is similar to that for the wedge. It has a higher percentage of g-term force with increasing the submerged depth.
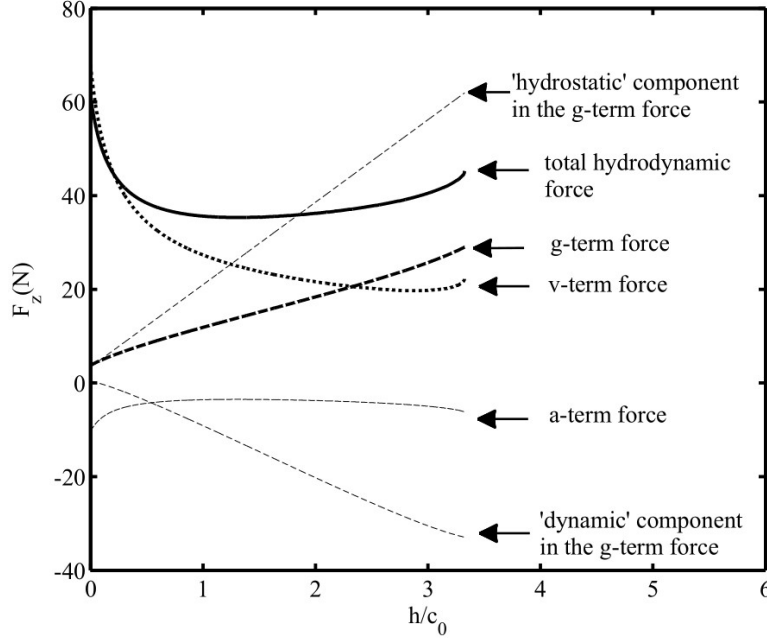
Fig. 3. Evolution of the unsteady force for the vertical water entry of the cone with deadrise angle 30°, initial entry speed 2.5m/s, half breadth 0.083m and mass 2.29 kg. The numerical simulation ends at the closure of the cavity; h is the distance between the top of the cone and the still water surface; c_0 is the half breadth of the cone.

B. g-term force

Wedge. First, we investigate the g-term force for the water entry of the wedges with the deadrise angle of β and the half breadth of c_0. A simplified model is introduced: a uniform open cavity behind the body is assumed; the free-surface boundary above the still water surface is transferred to the still water surface; the body boundary keep unchanged; and all corresponding boundary conditions are the same as the fully nonlinear case, i.e. follow Eqs. (13.b)-(13.d). The model is illustrated in Fig. 4. We will show that the g-term force is not sensitive to the cavity configuration and is well approximated by the simplified model. It should be noted that similar simplified models will be used for the g-term force of different body geometries and also for a-term forces.
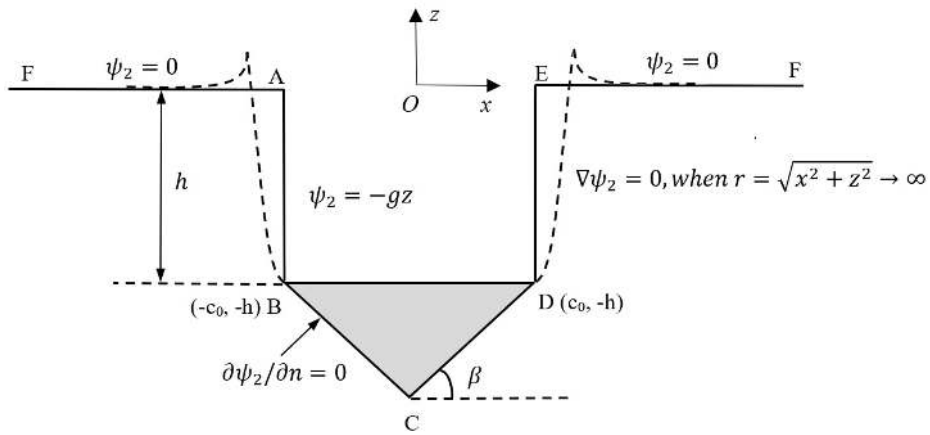

Fig. 4. Simplified model for estimating the g-term force of a wedge vertically entering the water surface. The real free-surface boundaries are represented by the dashed lines, which are replaced by the solid lines FAB and DEF in the simplified model.

Let $\phi = \psi_2 + gz$. Obviously, ψ_2 corresponds to the 'dynamic' component and gz the 'hydrostatic' component. Integrating ϕ over the wetted body surface results in the g-term force. ϕ satisfies the Laplace equation and the following boundary conditions

$$\phi = 0, \text{ on the free surface,} \tag{18.a}$$

$$\frac{\partial \phi}{\partial n} = -g \cos\beta, \text{ on the body boundary,} \tag{18.b}$$

$$\nabla\phi = g\mathbf{k} \text{ at } r = \sqrt{x^2 + z^2} \to \infty. \tag{18.c}$$

Here, $\mathbf{k}$ denotes the unit vector in the z direction. It notes that $h = 0$ results in a zero 'dynamic' component and a 'hydrostatic' component equal to the weight of the displaced water by the body. By the Schwarz-Christoffel transformation, the upper-half plane of ζ can be mapped into the fluid domain, $w = x + zi$, as presented in Fig. 5:

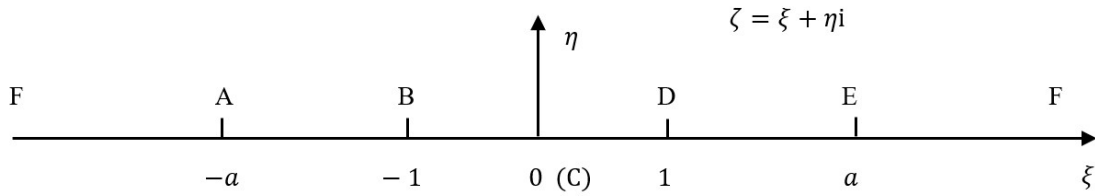$$w(\zeta) = C_1 + C_2 \int^\zeta \frac{(t^2-1)^{\frac{1}{2}-\frac{\beta}{\pi}} t^{2\beta/\pi}}{(t^2-a^2)^{1/2}} dt \ . \tag{19}$$

Fig. 5. The upper ζ-plane, mapped by the Schwarz-Christoffel transformation.

Here, the parameters a, C_1, and C_2 are determined by $w(0) = -\mathrm{i}(c_0 \tan\beta + h)$, $w(-1) = -c_0 - \mathrm{i}h$, $w(1) = c_0 - \mathrm{i}h$, $w(-a) = -c_0$, and $w(a) = c_0$. Then, we have

$$|C_2| = \frac{c_0/\cos\beta}{\int_0^1 \frac{(1-t^2)^{\frac{1}{2}-\frac{\beta}{\pi}} t^{2\beta/\pi}}{(a^2-t^2)^{1/2}} dt}, \tag{20}$$

$$h/c_0 = \frac{1}{\cos\beta} \frac{\int_1^a \frac{(t^2-1)^{\frac{1}{2}-\frac{\beta}{\pi}} t^{2\beta/\pi}}{(a^2-t^2)^{1/2}} dt}{\int_0^1 \frac{(1-t^2)^{\frac{1}{2}-\frac{\beta}{\pi}} t^{2\beta/\pi}}{(a^2-t^2)^{1/2}} dt}. \tag{21}$$

On the ζ-plane, ϕ satisfies the Laplace equation and the following boundary conditions

$$\phi = 0, \text{ on } (|\xi| > 1, 0), \tag{22.a}$$

$$\frac{\partial \phi}{\partial \eta} = -g \cos\beta \ |C_2| \frac{(1-\xi^2)^{\frac{1}{2}-\frac{\beta}{\pi}}}{(a^2-\xi^2)^{\frac{1}{2}}} \xi^{\frac{2\beta}{\pi}}, \text{ on } (|\xi| < 1, +0), \tag{22.b}$$

$$\nabla\phi = -|C_2| g\mathbf{k}, \text{ at } \zeta \to \infty. \tag{22.c}$$

ϕ can be split into $\phi = -|C_2|g\eta + \Phi$. Since $\eta = 0$ on the body surface, the term, $-|C_2|g\eta$, has no contribution to the g-term force. The function Φ satisfies the following boundary conditions

$$\Phi = 0, \text{ on } (|\xi| > 1, 0), \tag{23.a}$$

$$\frac{\partial \Phi}{\partial \eta} = g|C_2|\left(1 - \cos\beta \frac{(1-\xi^2)^{\frac{1}{2}-\frac{\beta}{\pi}}}{(a^2-\xi^2)^{\frac{1}{2}}} \xi^{\frac{2\beta}{\pi}}\right), \text{ on } (|\xi| < 1, +0), \tag{23.b}$$

$$\nabla\Phi = 0, \text{ at } \zeta \to \infty. \tag{23.c}$$

Let $\Phi = \Phi_1 + \Phi_2$, we have

$$\Phi_1 = 0, \text{ on } (|\xi| > 1, 0), \tag{24.a}$$

$$\frac{\partial \Phi_1}{\partial \eta} = g|C_2|, \text{ on } (|\xi| < 1, +0), \tag{24.b}$$

$$\nabla \Phi_1 = 0, at\ \zeta \to \infty\ , \tag{24.c}$$

and

$$\Phi_2 = 0, \text{ on } (|\xi| > 1, 0), \tag{24.d}$$

$$\frac{\partial \Phi_2}{\partial \eta} = -g \cos \beta \, |C_2| \frac{(1-\xi^2)^{\frac{1}{2}-\frac{\beta}{\pi}}}{(a^2-\xi^2)^{\frac{1}{2}}} \xi^{\frac{2\beta}{\pi}}, \text{ on } (|\xi| < 1, +0) \tag{24.e}$$

$$\nabla \Phi_2 = 0, at\ \zeta \to \infty. \tag{24.f}$$

On the body, i.e. $(|\xi| < 1, +0)$,

$$\Phi_1 = -g|C_2|\sqrt{1-\xi^2}. \tag{25}$$

Φ_2 can be represented as

$$\Phi_2(\xi, \eta) = \frac{1}{2\pi} PV \int_{-1}^{1} \gamma(t) \tan^{-1}\frac{\eta}{\xi-t} dt, \tag{26}$$

i.e. the vorticities on the line segment of $(|\xi| < 1, 0)$. The vortex strength $\gamma(t)$ is obtained by solving the following integral equation

$$\frac{1}{2\pi} PV \int_{-1}^{1} \frac{\gamma(t)}{\xi-t} dt = -g \cos \beta \, |C_2| \frac{(1-\xi^2)^{\frac{1}{2}-\frac{\beta}{\pi}}}{(a^2-\xi^2)^{\frac{1}{2}}} \xi^{\frac{2\beta}{\pi}} \quad for\ |\xi| < 1 \tag{27}$$

The solution for the homogeneous problem, corresponding to the right-hand-side of the above equation equal to zero, is $C/\sqrt{1-\xi^2}$. Here C is a constant and should be determined by some condition. Note that the distribution of the vortex strength is antisymmetric. It results in $C=0$. Let's change the variables as follows: $\xi = -\cos \chi$, $t = -\cos \theta$, and $\alpha(\theta) = \gamma(\xi) \sin \theta$. Then, we have an integral equation

$$\frac{1}{2\pi} PV \int_{0}^{\pi} \frac{\alpha(\theta)}{\cos \theta - \cos \chi} d\theta = -g \cos \beta \, |C_2| \frac{(1-(\cos \chi)^2)^{\frac{1}{2}-\frac{\beta}{\pi}}}{(a^2-(\cos \chi)^2)^{\frac{1}{2}}} (\cos \chi)^{\frac{2\beta}{\pi}}. \tag{28}$$

Inserting the Fourier expansion,

$$\alpha(\theta) = -2g \cos \beta \, |C_2| \sum_{n=1}^{\infty} a_n \cos(2n-1)\theta, \tag{29}$$

into Eq. (28), we obtain

$$\frac{1}{\pi} PV \int_{0}^{\pi} \frac{\sum_{n=1}^{\infty} a_n \cos(2n-1)\theta}{\cos \theta - \cos \chi} d\theta = \frac{(1-(\cos \chi)^2)^{\frac{1}{2}-\frac{\beta}{\pi}}}{(a^2-(\cos \chi)^2)^{\frac{1}{2}}} (\cos \chi)^{\frac{2\beta}{\pi}}. \tag{30}$$

This will require the evaluation of the Glauert integrals

$$\int_{0}^{\pi} \frac{\cos(2n-1)\theta}{\cos \theta - \cos \chi} d\theta = \pi \frac{\sin(2n-1)\chi}{\sin \chi}. \tag{31}$$

Then the integral equation (30) becomes

$$\sum_{n=1}^{\infty} a_n \sin(2n-1)\chi = \frac{(\sin \chi)^{2(1-\frac{\beta}{\pi})}}{(a^2-(\cos \chi)^2)^{\frac{1}{2}}} (\cos \chi)^{\frac{2\beta}{\pi}}.$$

The coefficients of the above Fourier series can be expressed as

$$a_n = \frac{2}{\pi} \int_{0}^{\pi} \frac{(\sin \chi)^{2(1-\frac{\beta}{\pi})}}{(a^2-(\cos \chi)^2)^{\frac{1}{2}}} (\cos^2 \chi)^{\frac{\beta}{\pi}} \sin(2n-1)\chi \, d\chi. \tag{32}$$

So far, we have the vortex distribution

$$\gamma(\xi) = \gamma(-\cos \theta) = -2g \cos \beta \, |C_2| \frac{1}{\sin \theta} \sum_{n=1}^{\infty} a_n \cos(2n-1)\theta. \tag{33}$$

The velocity potential on the body can be obtained:

$$\Phi_2(\xi, +0) = \int_{-1}^{\xi} \frac{\partial \Phi_2}{\partial t}(t, +0)dt = \int_{-1}^{\xi} -\frac{1}{2}\gamma(t)dt$$

$$= \int_0^{\chi} g\cos\beta \, |C_2| \sum_{n=1}^{\infty} a_n \cos(2n-1)\theta \, d\theta$$

$$= g\cos\beta \, |C_2| \sum_{n=1}^{\infty} \frac{a_n}{(2n-1)}\sin(2n-1)\chi. \tag{34}$$

The total velocity potential becomes

$$\Phi(\xi, +0) = -g\,|C_2|\sin\chi + g\cos\beta \, |C_2| \sum_{n=1}^{\infty} \frac{a_n}{(2n-1)}\sin(2n-1)\chi. \tag{35}$$

Thus, the vertical hydrodynamic force due to the gravity effect is written as

$$F_g = -\rho\cos\beta \int_{-c_0}^{c_0} \phi \, ds$$

$$= -\rho\cos\beta \int_{-1}^{1} \Phi(t, +0)|C_2| \frac{(1-t^2)^{\frac{1}{2}-\frac{\beta}{\pi}}}{(a^2-t^2)^{\frac{1}{2}}} t^{\frac{2\beta}{\pi}} dt$$

$$= \rho g|C_2|^2 \cos\beta \int_0^{\pi} \left\{ \sin\theta - \cos\beta \sum_{n=1}^{\infty} \frac{a_n}{(2n-1)}\sin(2n-1)\theta \right\} \frac{(\sin\theta)^{2(1-\frac{\beta}{\pi})}}{(a^2-(\cos\theta)^2)^{\frac{1}{2}}} (\cos\theta)^{\frac{2\beta}{\pi}} d\theta$$

$$= \frac{\pi}{2}\rho g|C_2|^2 \cos\beta \left\{ a_1 - \cos\beta \sum_{n=1}^{\infty} \frac{a_n^2}{(2n-1)} \right\}. \tag{36}$$

The series in the above equation converge very fast. The approximation,

$$F_g \approx \rho g|C_2|^2 \cos\beta \frac{\pi}{2}(a_1 - a_1^2\cos\beta), \tag{37}$$

is very close to the exact solution. Fig. 6 presents the solutions of the g-term forces at different deadrise angles. A larger deadrise angle results in a higher g-term force for a given submerged depth.
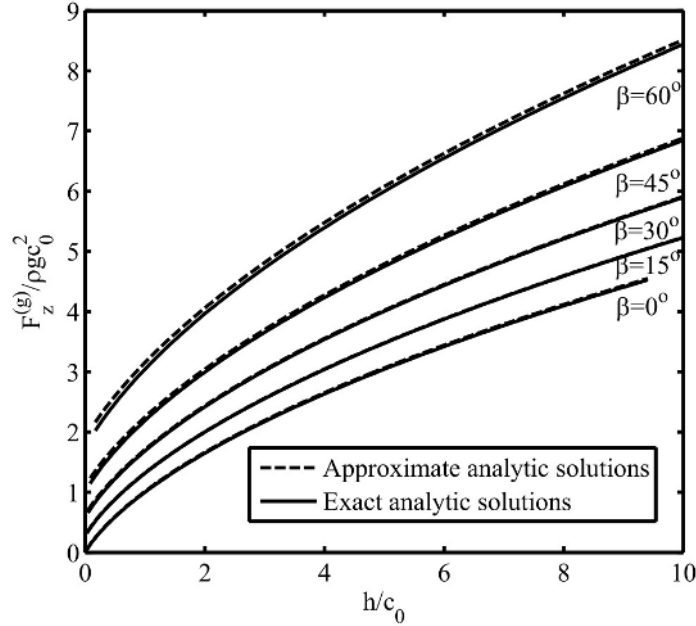

Fig. 6. Evolution of the g-term force of wedges vertically entering the water surface. It is predicted by the simplified model; h is the distance between the top of the wedge and the still water surface; c_0 is the half breadth of the wedge; the exact analytic solutions and the approximate analytic solutions are given

by Eq. (36) and Eq. (37) respectively.

Asymptotically ($a \rightarrow \infty$, corresponding to an infinite cavity), we have

$$h \approx a^2 \frac{c_0}{\cos \beta} A(\beta), \tag{38}$$

$$|C_2| \approx a \frac{c_0}{\cos \beta} A(\beta), \tag{39}$$

$$a_n \approx \frac{2}{\pi a} \int_0^{\pi} (\sin \chi)^{2(1-\frac{\beta}{\pi})} (\cos^2 \chi)^{\frac{\beta}{\pi}} \sin(2n-1)\chi \, d\chi \ , \tag{40}$$

$$\frac{F_g}{\rho g_0^{\frac{3}{2}}} \approx [A^{\frac{3}{2}}(\beta) B(\beta) (\cos \beta)^{-\frac{1}{2}}] \sqrt{\frac{h}{c_0}}, \tag{41}$$

where, $A(\beta) = 1/\int_0^{\pi/2} (\cos \chi)^{2(1-\frac{\beta}{\pi})} (\sin^2 \chi)^{\frac{\beta}{\pi}} d\chi$ and $B(\beta) = \int_0^{\pi} (\sin \chi)^{2(1-\frac{\beta}{\pi})} (\cos^2 \chi)^{\frac{\beta}{\pi}} \sin \chi \, d\chi$.

Eq. (41) indicates that for deeply submerged wedges the theoretical g-term force is linearly dependent on the square root of the submerged depth. This may be applied to other two-dimensional solid objects.

Numerical experiments are conducted to verify the simplified model of assuming a uniform cavity behind the falling body. The water-entry problem is solved in the time domain by the fully-nonlinear model presented in Section A. At each time step, the corresponding g-term force is evaluated after solving ψ_2, governed by (13.a)-(13.d), based on the exact free-surface boundary. The numerical solutions of the fully-nonlinear model are compared with the analytical solutions of the simplified model at the relatively small deadrise angle of $\beta = 30^\circ$ and at the relatively large deadrise angle of $\beta = 60^\circ$, as shown in Fig. 7. The agreement between the simplified model and the fully-nonlinear model confirms that the g-term force is not sensitive to the cavity shape. The key physical parameters of affecting the g-term are the projected wetted area, the submerged depth and the body geometry. It notes that $F_z^{(g)}(h=0)$ is equal to the weight of the water displaced by the body. Excluding this, the g-term force is not sensitive to the body geometry near the still water surface. The body geometry has a significant influence on the g-term force when the body is deeply submerged.
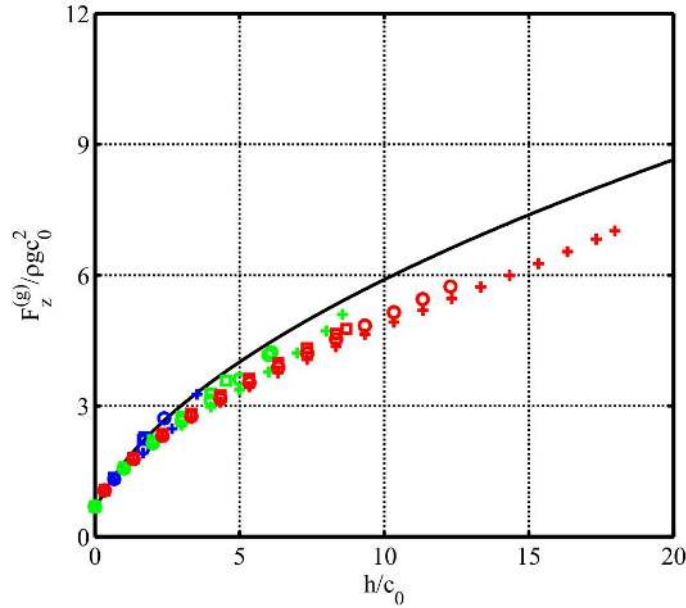
(a) $\beta = 30^\circ$
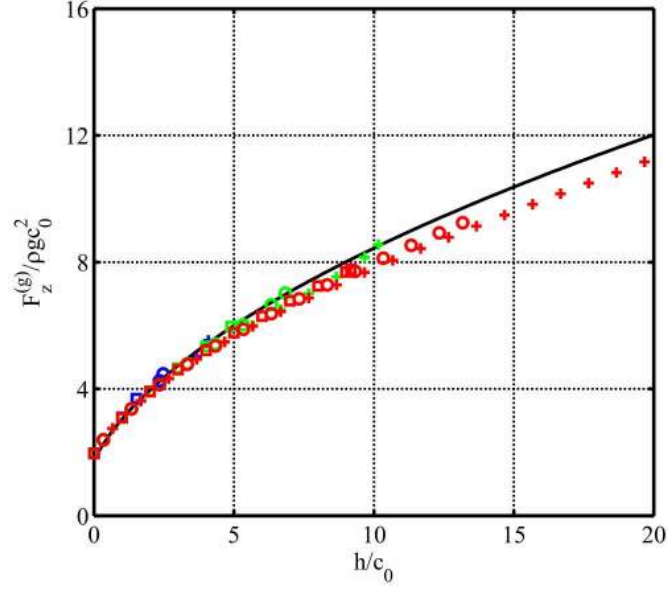
(b) $\beta = 60°$

Fig. 7. Comparison of the g-term force of wedges vertically entering the water surface. The solid lines represent the analytic solutions, of the simplified model, given by Eq. (36). The colored markers represent the numerical solutions of the fully-nonlinear model: the blue color denotes the mass ratio, $M/(0.5\rho\pi c_0^2)$, of 1, the green color denotes the mass ratio of 3, and the red color denotes the mass ratio of 9; the 'square' marker denotes the Froude number, $V_0/\sqrt{gc_0}$, of 2, the 'circle' marker denotes the Froude number of 4, the '+' marker denotes the Froude number of 8.

Flat plate. The flat plate corresponds the wedge with zero deadrise angle, i.e. $\beta = 0$. The Schwarz-Christoffel transformation is expressed as

$$w(\zeta)=-ih + C_2 \int_0^\zeta \sqrt{\frac{1-t^2}{a^2-t^2}}\, dt. \tag{42}$$

The parameters a and C_2 are determined by $w(1) = c_0 - ih$ and $w(a) = c_0$, which results in

$$c_0 = |C_2| \left[aE\left(\frac{1}{a}\right) - \frac{a^2-1}{a}K\left(\frac{1}{a}\right) \right], \tag{43}$$

$$h = |C_2| \left[aE\left(\frac{\sqrt{a^2-1}}{a}\right) - \frac{1}{a}K\left(\frac{\sqrt{a^2-1}}{a}\right) \right]. \tag{44}$$

K is the complete elliptic integral of the first kind and E is the complete elliptic integral of the second kind. a is the root of the following equation

$$h/c_0 = \frac{E\left(\frac{\sqrt{a^2-1}}{a}\right) - \frac{1}{a^2}K\left(\frac{\sqrt{a^2-1}}{a}\right)}{E\left(\frac{1}{a}\right) - \frac{a^2-1}{a^2}K\left(\frac{1}{a}\right)}. \tag{45}$$

The coefficient a_n becomes

$$a_n = \frac{2}{\pi} \int_0^\pi \frac{(\sin\chi)^2}{(a^2-(\cos\chi)^2)^{\frac{1}{2}}} \sin(2n-1)\chi \, d\chi. \tag{46}$$

The velocity potential on the body is

$$\Phi(\xi, +0) = -g|C_2| \sin\chi + g\,|C_2| \sum_{n=1}^\infty \frac{a_n}{(2n-1)} \sin(2n-1)\chi. \tag{47}$$

Further, the vertical force due to gravity can be expressed as

$$F_g = -\rho \int_{-1}^{1} \Phi(t,+0) |C_2| \sqrt{\frac{1-t^2}{a^2-t^2}} \, dt$$

$$= \rho g |C_2|^2 \int_0^\pi \left\{ \sin\theta - \sum_{n=1}^\infty \frac{a_n}{(2n-1)} \sin(2n-1)\theta \right\} (\sin\theta)^2 / (a^2 - (\cos\theta)^2)^{\frac{1}{2}} \, d\theta$$

$$= \rho g |C_2|^2 \frac{\pi}{2} \left\{ a_1 - \sum_{n=1}^\infty \frac{a_n^2}{(2n-1)} \right\}. \tag{48}$$

For small h/c_0, we have the following approximation

$$F_g \approx g|C_2|^2 \frac{\pi}{2} (a_1 - a_1^2) \text{ with } a_1 = \frac{2}{\pi} \left\{ \sqrt{a^2-1} + (2-a^2) \sin^{-1}(\frac{1}{a}) \right\}. \tag{49}$$

Cone. The above simplified model is generalized to the three-dimensional space for estimating the g-term force of the vertical water entry of cones. It is difficult to solve the three-dimensional model analytically but easy by the proposed boundary integral method. To avoid the infinite still water surface, an image flow above the undisturbed free surface is introduced as shown in Fig. 8, where, $\bar{z} = z/c_0$ is the dimensionless coordinate vertically upwards, $\bar{r} = r/c_0$ is the dimensionless radial coordinate and $\bar{\psi}_2 = \psi_2 / g c_0$.
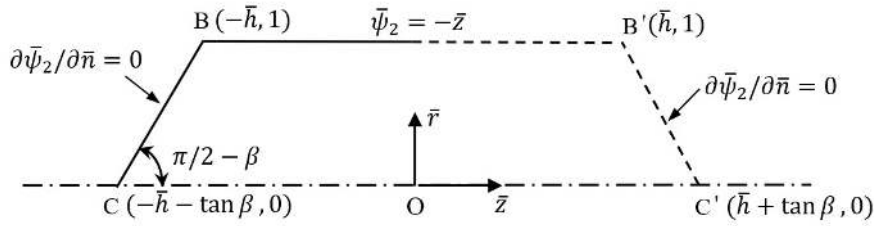

Fig. 8. Simplified model for estimating the dynamic component of the g-term force of a cone vertically entering the water surface.

Integrating ψ_2 over the wetted body surface will result in the 'dynamic' component in the g-term force. By including the 'hydrostatic' component, the g-term force is expressed as

$$\frac{F_g^{(z)}}{\pi \rho g c_o^3} = \underbrace{\left(\frac{\tan\beta}{3} + \bar{h} \right)}_{hydrostatic\ term} + \underbrace{\frac{1}{\pi} \int_{S_B} \bar{\psi}_2 \, n_z d\bar{s}}_{dynamic\ term}. \tag{50}$$

Excluding the weight of the water displaced by the body, i.e. $\tan\beta /3$, the g-term force is assumed to be

$$\bar{F}_g^{(z)} = \alpha \bar{h}^\gamma. \tag{51}$$

The numerical solutions, of the simplified model for the g-term force of the cones, at $1 < \bar{h} < 10$, are presented in Fig. 9, where $\bar{F}_g^{(z)} = [F_g^{(z)} - F_g^{(z)}(h=0)]/\pi \rho g c_o^3$. It can be seen that the g-term force indeed follows Eq. (51) and the coefficient, γ, corresponding to the slope of the solid line, is nearly independent on the deadrise angles. The coefficients, α and γ, at different deadrise angles are presented in Table 1. Similar to wedges, a larger deadrise angle results in a higher g-term force at a given submerged depth.
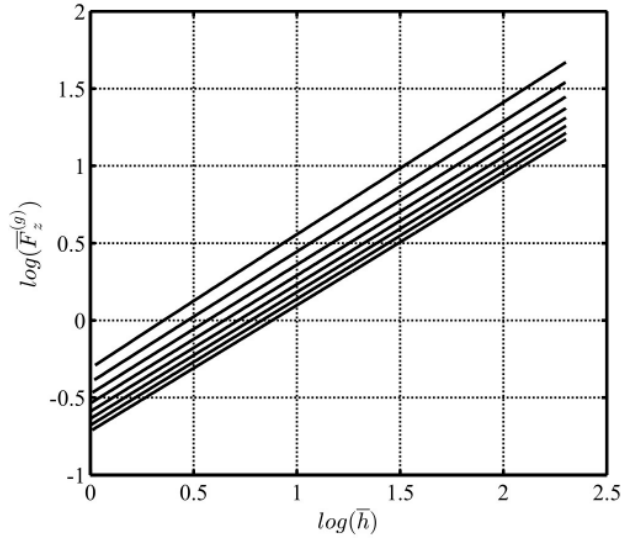
Fig. 9. The log-log plot of the g-term force, by the simplified model for cones vertically entering the water surface, over the submerged depth. $\bar{F}_g^{(z)} = \frac{F_g^{(z)}}{\pi \rho g c_0^3} - \frac{\tan \beta}{3}$ is the g-term force excluding the buoyance of the cone, i.e. the weight of the water displaced by the cone. The solid lines from bottom to top correspond to the deadrise angle 0°, 10°, 20°, 30°, 40°, 50°, 60°, and 70° respectively.

Table 1. Coefficients of the g-term force, represented as $\bar{F}_g^{(z)} = \alpha \bar{h}^\gamma$, for cones at the deadrise angle of β.

| $\beta(o)$	0	10	20	30	40	50	60	70
α	0.4860	0.5054	0.5274	0.5531	0.5838	0.6220	0.6714	0.7387
γ	0.8204	0.8216	0.8233	0.8257	0.8292	0.8345	0.8429	0.8575
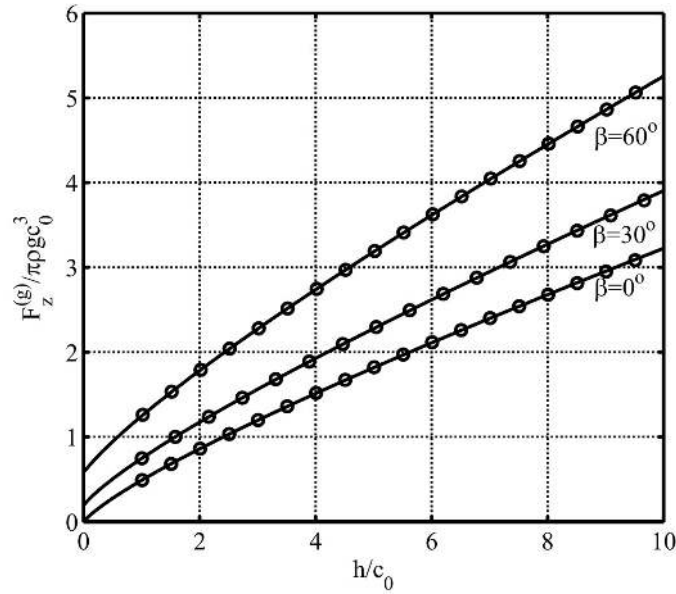
Fig. 10. Evolution of the g-term force of cones vertically entering the water surface. The solid lines denote the numerical solutions of the simplified model. The 'circle' markers denote the approximation of the numerical solutions by Eq. (51). β denotes the deadrise angle of the cone.

14 / 32

Numerical experiments, similar to those for wedges, are conducted to verify the simplified model. Fig. 11 presents the solutions of the fully-nonlinear model and the simplified model at the deadrise angle of 30° and 60°. Again, the simplified model gives the good approximation of the g-term force.

(a) $\beta = 30^o$

(b) $\beta = 60^o$
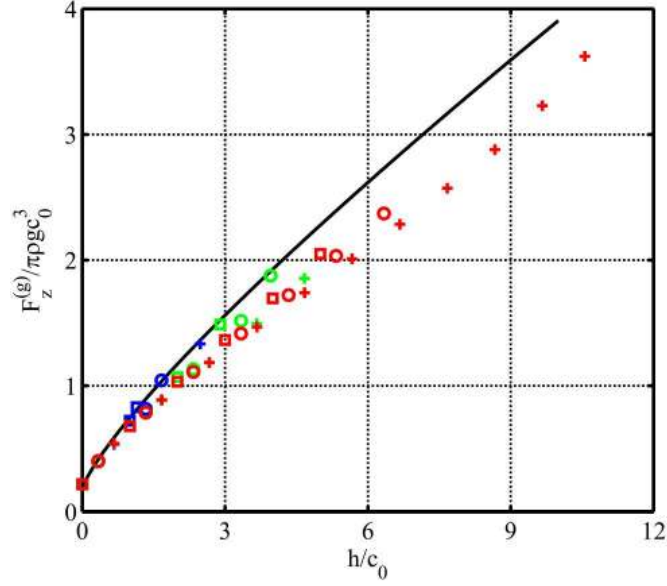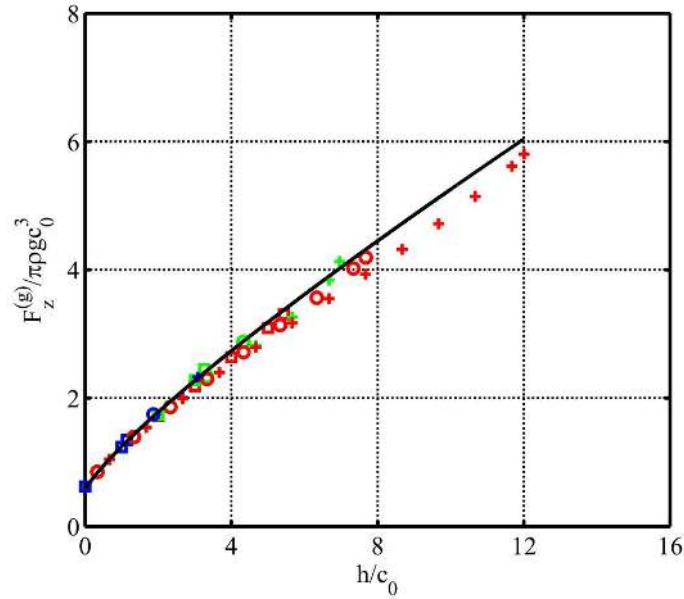
Fig. 11. Comparison of the g-term force of cones vertically entering the water surface. The solid lines represent the numerical solutions of the simplified model. The colored markers represent the numerical solutions of the fully-nonlinear model: the blue color denotes the mass ratio, $M/(4\rho\pi c_0^3/3)$, of 1, the green color denotes the mass ratio of 3, and the red color denotes the mass ratio of 9; the 'square' marker denotes the Froude number, $V_0/\sqrt{gc_0}$, of 2, the 'circle' marker denotes the Froude number of 4, the '+' marker denotes the Froude number of 8.

Circular cylinder. Fig. 12 illustrates the water entry of circular cylinders. The flow separates from the body at the angle of β_s. The steady cavity flow, past the circular cylinder, at zero cavitation number, results in the separation angle of about 55° and an infinite cavity.[34] It corresponds to the limiting state of a circular cylinder vertically entering the water surface with constant speed in a gravity-free environment. This section studies the g-term force at the flow separation angle from 55° to 90°, based on the simplified model assuming a uniform cavity behind the falling body. Fig. 13 shows the half of the simplified model, where the reference length c_0 is the half of the maximum wetted length equal to $R \sin \beta_s$.
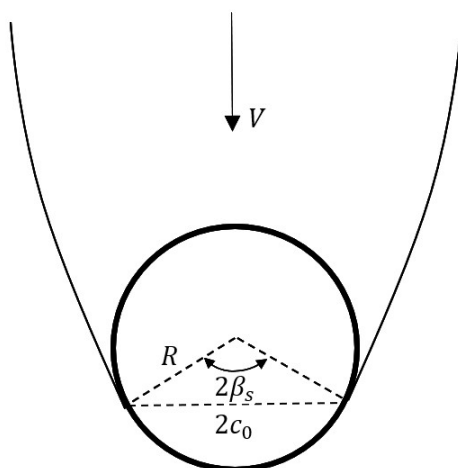

Fig. 12. Sketch of the water entry of a circular cylinder. R is the radius of the circular cylinder. β_s is the separation angle.
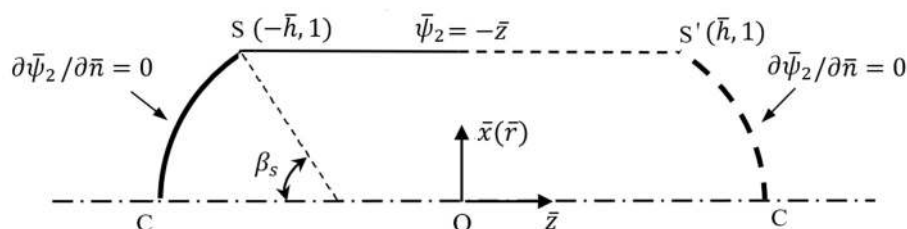

Fig. 13. Simplified model for estimating the dynamic component of the g-term force of a circular cylinder/sphere vertically entering the water surface. β_s is the flow separation angle.

Fig. 14 compares the g-term force between circular cylinders and wedges. It is observed that, for a given flow separation angle of the circular cylinder, there is a wedge with some deadrise angle resulting in the good approximation of the g-term force. Table 2 suggests using the g-term force of the wedge of the deadrise angle of β to approximate that of the circular cylinder with the flow separation angle of β_s.
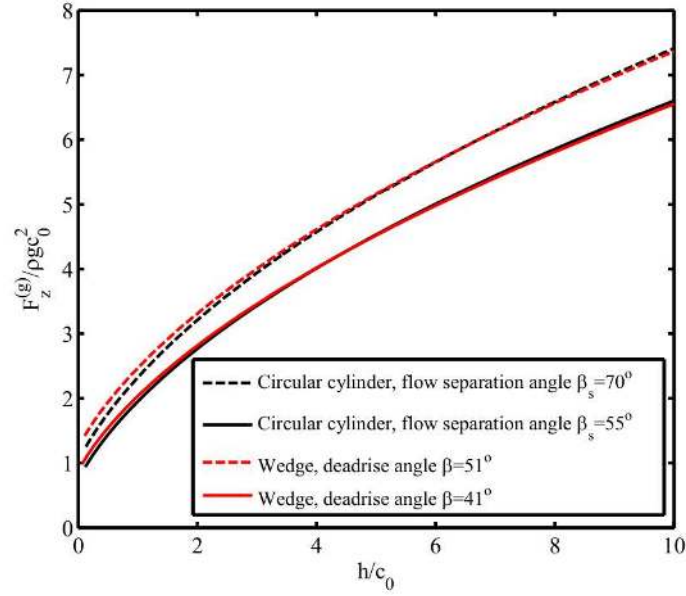
Fig. 14. Comparison of the g-term force between wedges and circular cylinders.

Table 2. Approximating the g-term force of the circular cylinder with the flow separation angle β_s by that of the wedge with the deadrise angle β.

β_s (deg)	55	60	65	70	75	80	85	90
β (deg)	41	45	48	51	54	57	60	63

Sphere. The g-term force of spheres is estimated by the simplified model presented in Fig. 13. The solutions of the simplified model may also follow Eq. (51), which is confirmed by the log-log plot of the g-term force over $\bar{h}$ as shown in Fig. 15. The coefficients, α and γ, at the flow separation angle from 55° to 90° are presented in Table 3. It is observed that γ is weekly dependent on the flow separation angle and is close to that of cones.
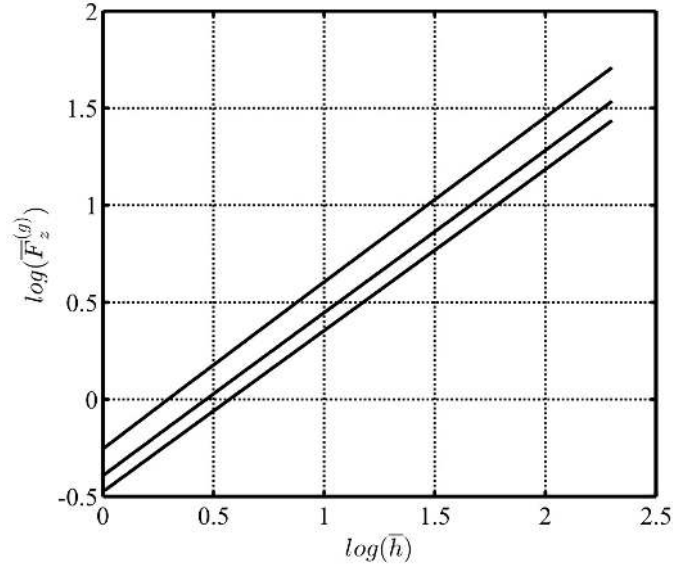

Fig. 15. The log-log plot of the g-term force, by the simplified model for spheres vertically entering the water surface, over the submerged depth. $\bar{F}_g^{(z)} = [F_g^{(z)} - F_g^{(z)}(h = 0)]/\pi\rho g c_o^3$ is the dimensionless g-term force excluding the weight of the water displaced by the sphere. The solid lines from bottom to top correspond to the flow separation angle 55°, 70°, and 90° respectively.

Table 3. Coefficients of the g-term force, represented as $\bar{F}_g^{(z)} = \alpha \bar{h}^\gamma$, for spheres with the flow separation angle of β_s.

β_s(o)	55	60	65	70	75	80	85	90
α	0.6214	0.6383	0.6567	0.6768	0.6990	0.7234	0.7505	0.7806
γ	0.8298	0.8317	0.8338	0.8362	0.8390	0.8423	0.8460	0.8503
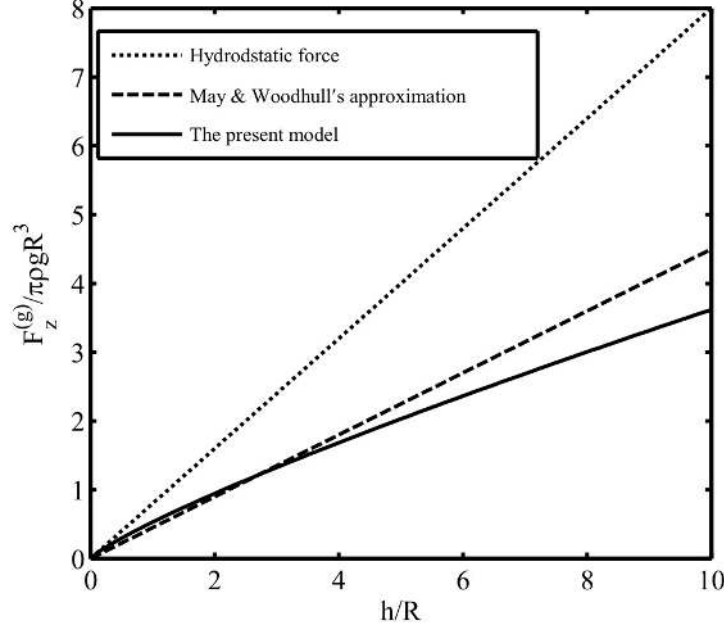
Fig. 16. Comparison between May & Woodhull's approximation[35] and the present model for the g-term force.

May & Woodhull investigated the drag coefficients of steel spheres entering water vertically.[35] For the evaluation of the drag coefficient defined by the V-squared law, they excluded all forces having a different independence on V and expressed the equation of motion of the body as Eq. (1). It notes that the term ρghS in Eq. (1) corresponds to the hydrostatic force obtained by directly integrating the hydrostatic term in the Bernoulli's equation over the wetted body surface (here, the weight of the water displaced by the sphere is excluded). Their analysis used $S = 0.45\pi R^2$ instead of the measured value $0.8\pi R^2$ (R is the radius of the sphere) for the evaluation of ρghS, giving satisfactory results. The projected wetted area of $0.8\pi R^2$ corresponds to the flow separation angle β_s of about 65º. Fig. 16 shows that the hydrostatic force strongly overestimates the force due to the gravity effect. May & Woodhull's approximation is close to the present solution throughout the early part of the sphere's trajectory, where the drag coefficient is reasonably constant and was studied.[35]

C. a-term force

The a-term force is proportional to the body acceleration and can be written as $F_z^{(a)} = -A_{33}\dot{V}$. A_{33} represents the high-frequency add mass of the body in the vertical direction and is expressed as

$A_{33} = \rho \int_{S_B} \bar{\psi}_1 n_z \, ds$, where $\bar{\psi}_1$ is the solution of the following equations

$$\nabla^2 \bar{\psi}_1 = 0 \ \text{in} \ \Omega, \tag{52.a}$$

$$\bar{\psi}_1 = 0 \ \text{on} \ S_F, \tag{52.b}$$

$$\frac{\partial \bar{\psi}_1}{\partial n} = -n_z \ \text{on} \ S_B, \tag{52.c}$$

$$\bar{\psi}_1 \to 0 \ \text{at} \ |X| \to \infty. \tag{52.d}$$

Wedge. By assuming a uniform open cavity behind the body and following the procedure presented in the previous analysis, we can express the added mass for wedges as

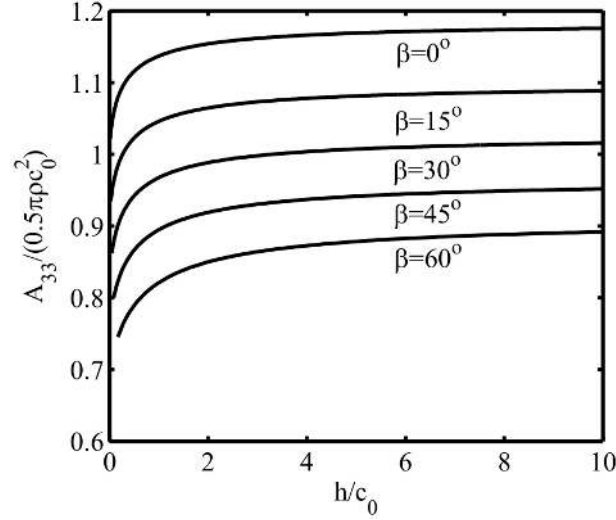$$A_{33}/(\frac{\pi}{2}\rho c_0^2) = \frac{1}{c_0^2}|C_2|^2\cos^2\beta \sum_{n=1}^{\infty} \frac{a_n^2}{(2n-1)}. \tag{53}$$

Fig. 17. Evolution of the added mass predicted by the simplified model for wedges vertically entering the water surface. β is the deadrise angle of the wedges.

Fig. 17 presents the evolution of the vertical added mass predicted by the simplified model. With increasing the submerged depth, the added mass grows strongly near the undisturbed free surface and quickly approaches the value of $h = \infty$. At $h = 0$ (corresponding to $a = 1$), A_{33} is expressed as

$$A_{33}(h = 0)/(\frac{\pi}{2}\rho c_0^2) = (\frac{2}{\pi})^2 \sum_{n=1}^{\infty} \frac{1}{2n-1}\left[\frac{\int_0^\pi (\sin\chi)^{\left(1-\frac{2\beta}{\pi}\right)}(\cos^2\chi)^{\frac{\beta}{\pi}}\sin(2n-1)\chi d}{\int_0^{\pi/2}(\cos\chi)^{\left(1-\frac{2\beta}{\pi}\right)}(\sin^2\chi)^{\frac{\beta}{\pi}}d\chi}\right]^2. \tag{54}$$

It is easy to verify $A_{33}(h = 0) = \pi\rho c_0^2/2$ for $\beta = 0^o$, which is exactly the high-frequency added mass of the flat plate. Letting $h \to \infty$, we have $a \to \infty$ and $(a^2 - (\cos\chi)^2)^{1/2} \approx a$. Then, the added mass becomes

$$A_{33}(h = \infty)/(\frac{\pi}{2}\rho c_0^2) = (\frac{2}{\pi})^2 \sum_{n=1}^{\infty} \frac{1}{2n-1}\left[\frac{\int_0^\pi (\sin\chi)^{2\left(1-\frac{\beta}{\pi}\right)}(\cos^2\chi)^{\frac{\beta}{\pi}}\sin(2n-1)\chi d\chi}{\int_0^{\pi/2}(\cos\chi)^{2\left(1-\frac{\beta}{\pi}\right)}(\sin^2\chi)^{\frac{\beta}{\pi}}d\chi}\right]^2. \tag{55}$$

The added mass of $h = 0$ and $h = \infty$ from $\beta = 0^o$ to $\beta = 80^o$ is presented in Fig. 18.
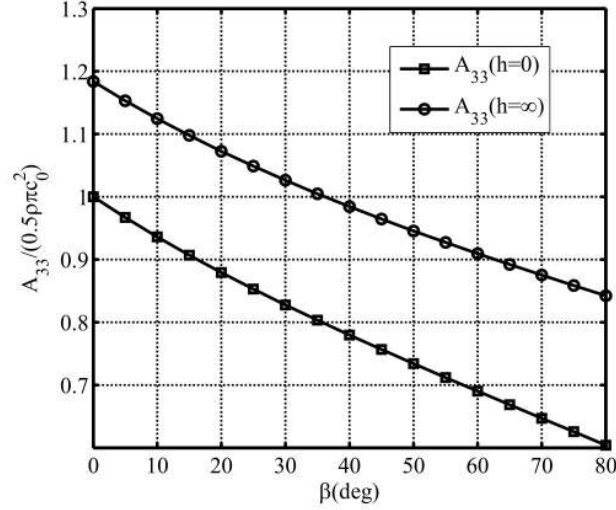
Fig. 18. Added mass, at $h = 0$ and $h = \infty$, for wedges vertically entering the water surface. β is the deadrise angle of the wedges.

Numerical experiments are conducted to verify the added mass predicted by the simplified model of assuming a uniform cavity behind the falling body. The water-entry problem is solved in the time domain by the fully-nonlinear model presented in Section A. At each time step, the corresponding added mass is evaluated after solving $\bar{\psi}_1$, governed by (52.a)-(52.d), based on the exact free-surface boundary. The numerical solutions of the fully-nonlinear model are compared with the analytical solutions of the simplified model at the deadrise angle of $\beta = 30^\circ$ and $\beta = 60^\circ$, as shown in Fig. 19. It confirms that the added mass grows strongly near the undisturbed free surface with increasing the submerged depth. The simplified model accurately predicts the added mass of the wedges near the still water surface and may overestimate that of the deeply submerged wedge (about 6%). The key physical parameters of affecting the added mass are the body geometry and the submerged depth.
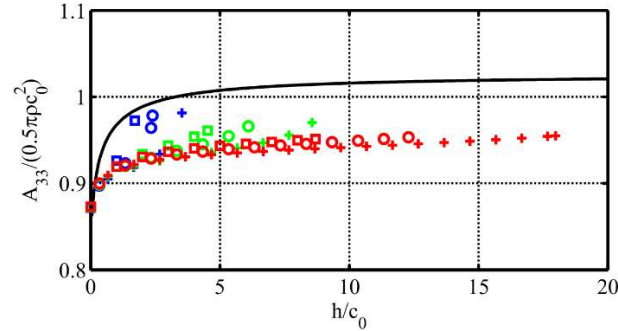
(a) $\beta = 30^\circ$
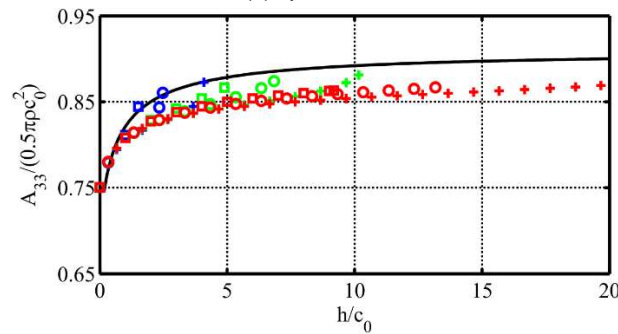
(b) $\beta = 60^\circ$

Fig. 19. Comparison of the added mass of wedges vertically entering the water surface. The solid lines represent the analytic solutions, of the simplified model, given by Eq. (53). The colored markers represent the numerical solutions of the fully-nonlinear model: the blue color denotes the mass ratio, $M/(0.5\rho\pi c_0^2)$, of 1, the green color denotes the mass ratio of 3, and the red color denotes the mass ratio of 9; the 'square' marker denotes the Froude number, $V_0/\sqrt{gc_0}$, of 2, the 'circle' marker denotes the Froude number of 4, the '+' marker denotes the Froude number of 8.

Cone. The simplified model is generalized to the three-dimensional space for estimating the added mass of the vertical water entry of cones. Again, an image flow above the undisturbed free surface is introduced as shown in Fig. 20, where, $\bar{z} = z/c_0$ is the dimensionless coordinate vertically upwards and $\bar{r} = r/c_0$ is the dimensionless radial coordinate. φ can be solved by the boundary integral method and then the added mass is evaluated by $A_{33}/(\frac{4}{3}\rho c_0^3) = \frac{3}{4}\int_{S_B} \bar{\psi}_1 n_z\, ds$.
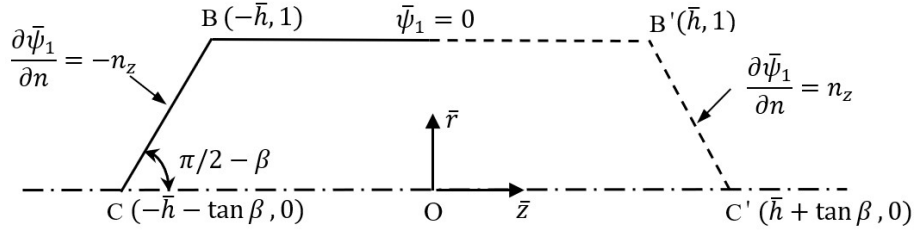

Fig. 20. Simplified model for estimating the added mass of a cone vertically entering the water surface.

The evolution of the vertical added mass of cones, presented in Fig. 21, is similar to that of wedges. It is noticed that the added mass of cones approaches the value of $h = \infty$ more quickly with increasing the submerged depth. The added mass of $h = 0$ and $h/c_0 = 20$ from $\beta = 0°$ to $\beta = 80°$ is presented in Fig. 22. For a given deadrise angle, the difference between the added mass of $h = 0$ and the added mass of $h/c_0 = 20$ is smaller than that of wedges. The added mass of cones is more sensitive to the deadrise angle, comparing to wedges.
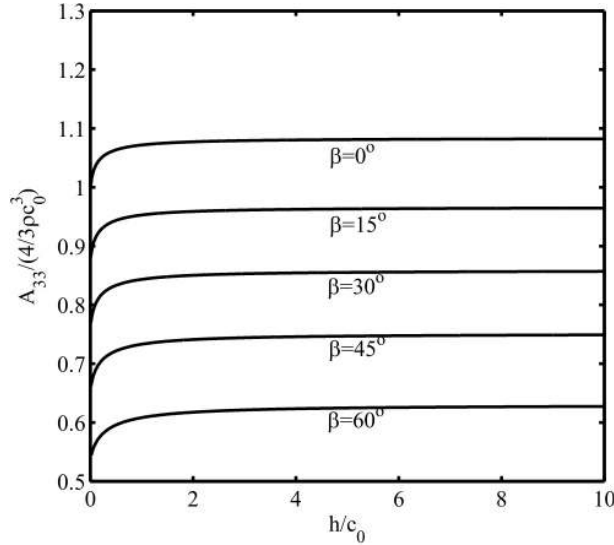

Fig. 21. Evolution of the added mass predicted by the simplified model for cones vertically entering the water surface. β is the deadrise angle of the cones.
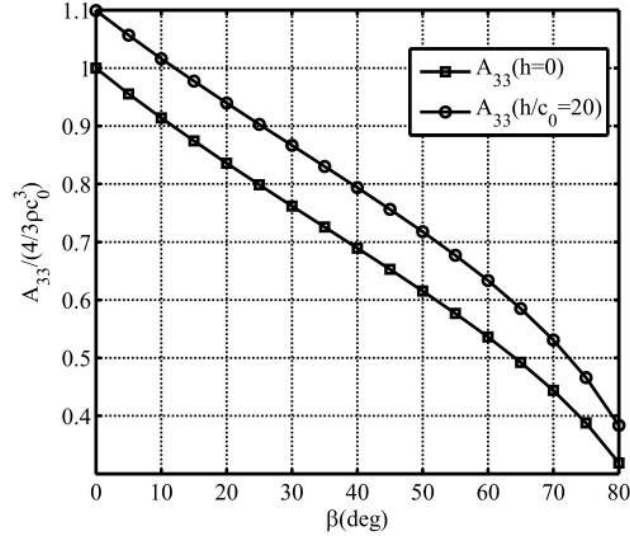
Fig. 22. Added mass, at $h = 0$ and $h/c_0 = 20$, for cones vertically entering the water surface. β is the deadrise angle of the cones.

Numerical experiments are conducted to verify the added mass predicted by the simplified model of assuming a uniform cavity behind the falling body. The fully-nonlinear model is solved in the time domain by the numerical method presented in Section A, which results in the exact cavity configuration and added mass. The numerical solutions of the fully-nonlinear model are compared with the analytical solutions of the simplified model at the deadrise angle of $\beta = 30^\circ$ and $\beta = 60^\circ$, as shown in Fig. 23. It confirms that the added mass grows strongly near the undisturbed free surface with increasing the submerged depth. The simplified model accurately predicts the added mass of the cones near the still water surface and may slightly (less than 5%) overestimate that of the deeply submerged cone. It notes that the predicted added mass of the disk on the free surface, i.e. $A_{33}(h = 0)$ at $\beta = 0^\circ$, agrees with Glasheen & McMahon 's experiments.[11] The key physical parameters of affecting the added mass are the body geometry and the submerged depth. $[A_{33}(h = 0) + A_{33}(h = \infty)]/2$ can be used as the first approximation of the added mass of the cone at any submerged depth.
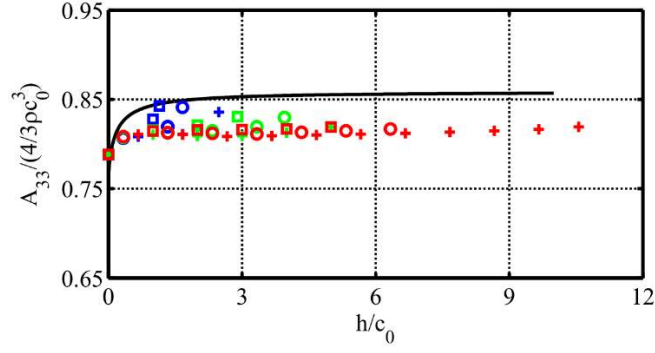
(a) $\beta = 30°$
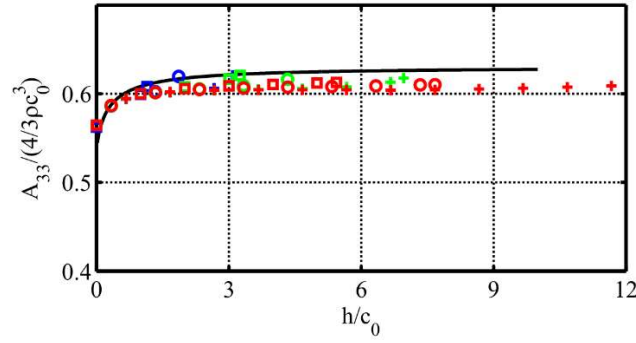
(b) $\beta = 60°$

Fig. 23. Comparison of the added mass of cones vertically entering the water surface. β is the deadrise angle of the cones. The solid lines represent the numerical solutions of the simplified model. The colored markers represent the numerical solutions of the fully-nonlinear model: the blue color denotes the mass ratio, $M/(4\rho c_0^3/3)$, of 1, the green color denotes the mass ratio of 3, and the red color denotes the mass ratio of 9; the 'square' marker denotes the Froude number, $V_0/\sqrt{gc_0}$, of 2, the 'circle' marker denotes the Froude number of 4, the '+' marker denotes the Froude number of 8.

Circular cylinder and sphere. The simplified model for estimating the added mass is presented in Fig. 24, where the reference length c_0 is the half of the maximum wetted length equal to $R\sin\beta_s$. The flow separates from the body at S resulting in the flow separation angle of β_s. A uniform cavity is assumed behind the body. An image flow above the undisturbed free surface is introduced.
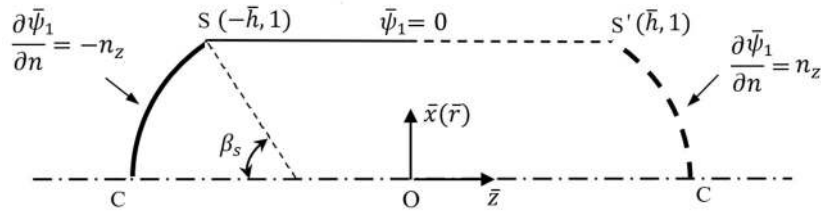

Fig. 24. Simplified model for estimating the added mass of a circular cylinder/sphere vertically entering the water surface.

The evolution of the vertical added mass of circular cylinders/spheres can be shown being similar to that of wedges/cones: with increasing the submerged depth, the added mass grows strongly near the undisturbed free surface and quickly approaches the value of $h = \infty$. Table 4 presents the dimensionless

added mass of circular cylinders and spheres on the still water surface, i.e. $\bar{h} = 0$ and at a deeply-submerged depth of $\bar{h} = 20$. $\bar{A}_{33} = 1$, i.e. $A_{33} = \pi\rho c_0^2/2$ for circular cylinder and $A_{33} = \pi\rho c_0^3/3$ for spheres, can be used as the first approximation of the added mass at any submerged depth.

Table 4. Dimensionless added mass of circular cylinders and spheres. β_s is the flow separation angle. The dimensionless added mass is defined as $\bar{A}_{33} = A_{33}/(\frac{\pi}{2}\rho c_0^2)$ for cylinders and $\bar{A}_{33} = A_{33}/(\frac{\pi}{3}\rho c_0^3)$ for spheres.

Circular cylinder							
β_s(o)	55	60	65	70	75	80	85	90
$\bar{A}_{33}(\bar{h}=0)$	0.891	0.894	0.901	0.910	0.924	0.942	0.967	1.000
$\bar{A}_{33}(\bar{h}=20)$	1.104	1.110	1.119	1.132	1.149	1.173	1.203	1.241
Sphere							
β_s(o)	55	60	65	70	75	80	85	90
$\bar{A}_{33}(\bar{h}=0)$	0.975	0.963	0.954	0.949	0.950	0.958	0.974	1.000
$\bar{A}_{33}(\bar{h}=20)$	1.113	1.100	1.090	1.085	1.084	1.090	1.103	1.126

D. v-term force

Through the definition of the v-term force, i.e. $F_z^{(v)} = \rho \int_{S_B}(\psi_3 - \mathbf{V}\cdot\nabla\varphi + \frac{1}{2}|\nabla\varphi|^2)n_z\,ds$ and the governing equations of ψ_3, it is natural to express the dimensionless v-term force as $C_v = F_z^{(v)}/(0.5\rho V^2 S)$. Here, S is the area of the maximum cross section of the falling body. C_v may be called as the 'velocity-drag coefficient'. Fig. 25 illustrates the typical evolution of the velocity-drag coefficient of wedges vertically entering the water surface until the cavity pinch-off. At the early stage, C_v is decreasing strongly with increasing the submerged depth. At the very early stage, i.e. near the still water surface, C_v is independent of the mass ratio and Froude number. After the submerged depth is greater than a few characteristic lengths, C_v evolves gently. During this stage, C_v is reasonably constant and overestimates the steady-state value, corresponding to an infinite open cavity and a constant drag coefficient.[33] It notes that the steady state is the limiting state of a wedge entering the water surface vertically with a constant speed in a zero-gravity environment (equivalent to the infinite Froude number). Therefore, C_v is closer to the steady-state value for the larger Froude number. The duration of this stage becomes longer for the larger mass ratio. Close to the pinch-off of the open cavity, C_v is growing strongly especially for small mass ratios. These physical phenomena will be discussed qualitatively.
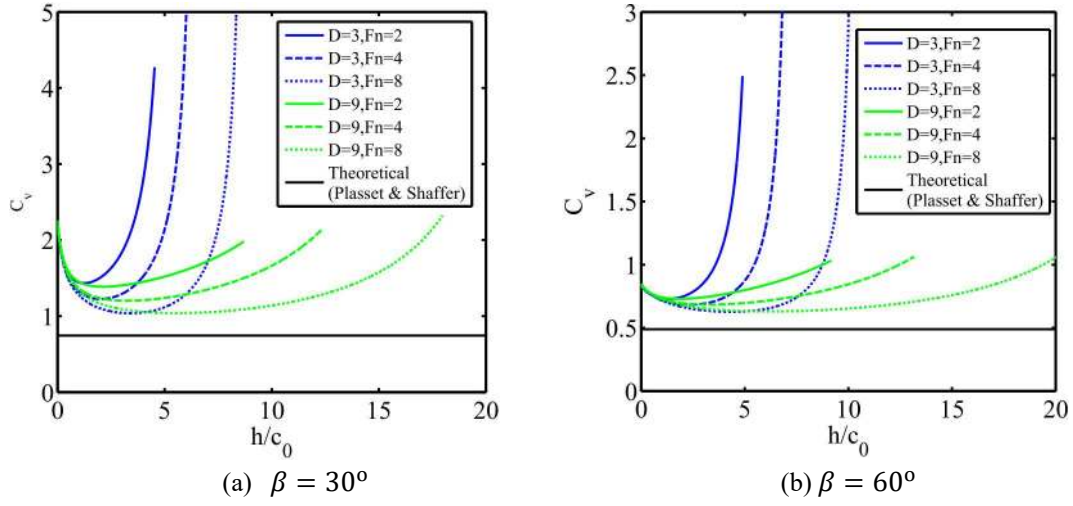
(a) $\beta = 30°$ (b) $\beta = 60°$

Fig. 25. Evolution of the velocity-drag coefficient of the wedge with the deadrise angle of β vertically entering the water surface until the cavity pinch-off. $D = M/0.5\rho\pi c_0^2$ is the mass ratio. $Fn = V_0/\sqrt{gc_0}$ is the Froude number. The blue and green lines indicate the numerical solutions of the fully nonlinearly model.

Instead of solving ψ_3, we consider an equivalent problem, $\tilde{\psi}_3 = \psi_3 - \mathbf{V} \cdot \nabla\varphi$. Based on Eqs. (14.a)-(14.d), $\tilde{\psi}_3$ can be decomposed into $\tilde{\psi}_3 = \psi_3^{(1)} + \psi_3^{(2)}$, which satisfies the following equations

$$\nabla^2 \psi_3^{(1)} = 0 \ \text{in} \ \Omega, \tag{56.a}$$

$$\psi_3^{(1)} = -\frac{1}{2}|\nabla\varphi|^2 \ \text{on} \ S_F, \tag{56.b}$$

$$\frac{\partial \psi_3^{(1)}}{\partial n} = 0 \ \text{on} \ S_B, \tag{56.c}$$

$$\psi_3^{(1)} \to 0 \ \text{at} \ |\mathbf{X}| \to \infty, \tag{56.d}$$

and

$$\nabla^2 \psi_3^{(2)} = 0 \ \text{in} \ \Omega, \tag{57.a}$$

$$\psi_3^{(2)} = 0 \ \text{on} \ S_F, \tag{57.b}$$

$$\frac{\partial \psi_3^{(2)}}{\partial n} = -\frac{\partial}{\partial n}(\mathbf{V} \cdot \nabla\varphi) \ \text{on} \ S_B, \tag{57.c}$$

$$\psi_3^{(2)} \to 0 \ \text{at} \ |\mathbf{X}| \to \infty. \tag{57.d}$$

Then, we have

$$F_z^{(v)} = \underbrace{\rho \int_{S_B} (\psi_3^{(1)} + \frac{1}{2}|\nabla\varphi|^2) n_z \, ds}_{F^{(1)}} + \underbrace{\rho \int_{S_B} \psi_3^{(2)} n_z \, ds}_{F^{(2)}}. \tag{58}$$

When the water-entry problem is solved in the time domain by the fully-nonlinear model presented in Section A, $\psi_3^{(1)}$ and $\psi_3^{(2)}$ can be evaluated by the boundary integral method based on the exact free-surface boundary at each time step, resulting in the numerical evolution of $F^{(1)}$, $F^{(2)}$ and $F_z^{(v)}$.
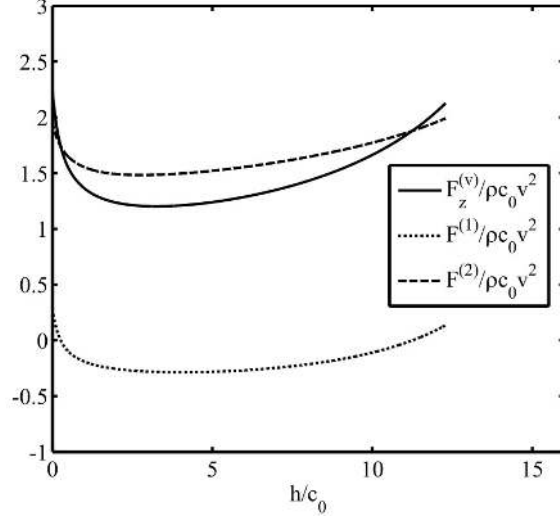
Fig. 26. Numerical evolution of $F^{(1)}$, $F^{(2)}$ and $F_z^{(v)}$ for the wedge with $Fn = 4$, $D = 9$ and $\beta = 30°$ vertically entering the water surface until the cavity pinch-off. $D = M/0.5\rho\pi c_0^2$ is the mass ratio; $Fn = V_0/\sqrt{gc_0}$ is the Froude number; β is the deadrise angle.

Fig. 26 illustrates the evolution of $F^{(1)}$, $F^{(2)}$ and $F_z^{(v)}$ for a wedge vertically entering the water surface. It can be seen that $F^{(2)}$ is the dominant component of $F_z^{(v)}$. This fact tends to be confirmed by our numerical results of other combinations of Froude number, mass ratio and deadrise angle for the wedge/cone vertically entering the water surface.

Eq. (57.c) is the unique non-trivial boundary condition for $\psi_3^{(2)}$. Therefore, the solution of $\psi_3^{(2)}$ and the corresponding C_v strongly depend on Eq. (57.c), which is related to the velocity field near the wetted body and characterized by the body shape and the shape of the attached open cavity. The cavity dynamics of solid objects vertically entering the water surface have been extensively investigated,[4-6, 11, 24-32] since Worthington & Cole's work[26]. Here, we only outline several aspects for the further discussion. If the water-entry speed is sufficiently large, an air cavity will be created behind the falling body.[7] The cavity expands at the beginning and the gravity effect resists the expansion of the cavity causing its contraction and pinch-off (closure).[25] This procedure is illustrated by Fig. 27. The slenderness of the closed cavity is characterized by the ratio, $2c_0/l$. In general, larger mass ratios of the falling body result in slenderer closed cavities.[32,40]
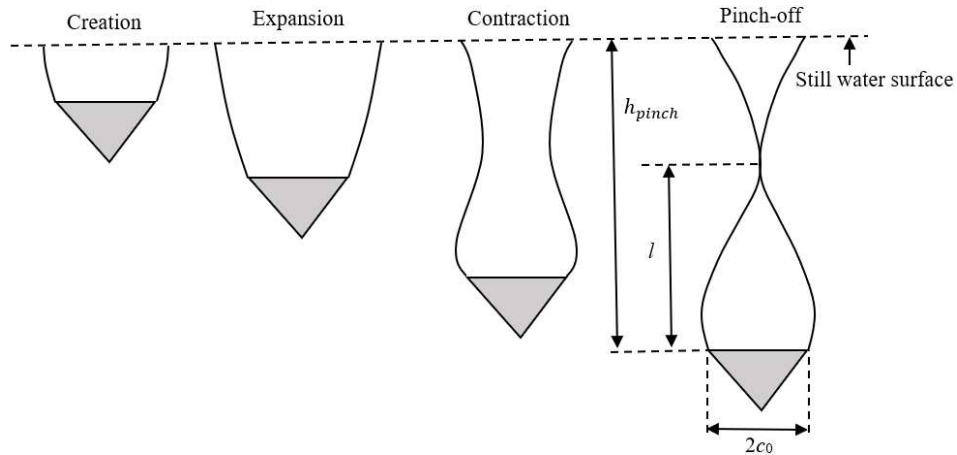

Fig. 27. Illustration of the evolution of the air cavity for a wedge vertically entering the water surface until the cavity pinch-off. The slenderness of the closed cavity is characterized by the ratio, $2c_0/l$.

For the velocity-drag coefficient defined by the V-squared law, the non-dimensional boundary condition, i.e. $[-\partial(\mathbf{V} \cdot \nabla\varphi)/\partial n]/V^2$, should be considered. It can be shown that,

$$-\frac{\partial(\mathbf{V}\cdot\nabla\varphi)/\partial n}{V^2}=cos\beta\,\frac{\partial}{\partial s}\left[\frac{\partial\varphi/\partial s}{V}\right] \tag{59}$$

for wedges. Here s refers to the tangential direction. The right-hand side of Eq. (59) is $cos\beta$ times the variation of the dimensionless tangential velocity along the wetted body surface. At the apex of the wedge, the dimensionless tangential velocity is fixed to be $-\sin\beta$ throughout the water-entry process. Near the still water surface, the water particle leaves the knuckle point somehow 'freely'. For smaller deadrise angles, both $cos\beta$ and the detaching speed are larger, resulting in the stronger variation of the dimensionless tangential velocity and therefore greater C_v. At the very early stage, the gravity effect is commonly negligible. So, the flow is not sensitive to the mass ratio and Froude number and $C_v(h=0)$ can be regarded to be a constant for a given body. With increasing the submerged depth, the effect of the surrounding water constraining the detaching speed becomes stronger, which leads to the weaker variation of the dimensionless tangential velocity and therefore the decreasing of C_v. This effect tends to be steady after the submerged depth is greater than a few characteristic lengths. Then C_v is not sensitive to the increment of the submerged depth. The evolution of C_v goes to the second stage. During that C_v is reasonably constant. If the air cavity continues the expansion, the second stage is lasting and C_v will slowly approach the limiting value presented by Plasset & Shaffer[33]. The expansion of the air cavity is of relevance to the strong transferring of the energy from the falling body to the water. This process becomes longer for the falling body with higher energy, i.e. larger mass ratio and/or higher Froude number, which results in the longer second stage of the evolution of C_v. Fig. 25 has shown that the second stage is very short or even obscure for the wedge with relatively small mass ratio/ Froude number. The gravity resists the expansion of the cavity causing its contraction and pinch-off.[24, 30] The contraction of the open cavity influences the evolution of C_v through modifying the velocity field near the wetted body. The numerical experiments show that the contraction of the air cavity strengthens the variation of the tangential velocity along the wetted wedge surface. Closer to the pinch-off, this effect becomes stronger. Further, smaller mass ratios result in blunter closed cavities[32,40] and therefore the stronger variation of the velocity field near the wetted body. So, C_v for the objects with small mass ratios evolves dramatically close to the pinch-off of the open cavity. These analyses are confirmed by Fig. 28, which plots the variation of the tangential velocity along the wetted body surface of the wedge, predicted by the fully nonlinear numerical method. At $h=0$, the good agreement of the tangential velocity is consistent with the good agreement of C_v as shown in Fig. 25. At $h=h_{pinch}/2$(within the second stage), the variation of the tangential velocity becomes closer to the theoretical value,[33] corresponding to C_v closer to the theoretical value. At the pinch-off of the cavity, the variation of the tangential velocity is strong especially for the small mass ratio, which results in the large value of C_v.
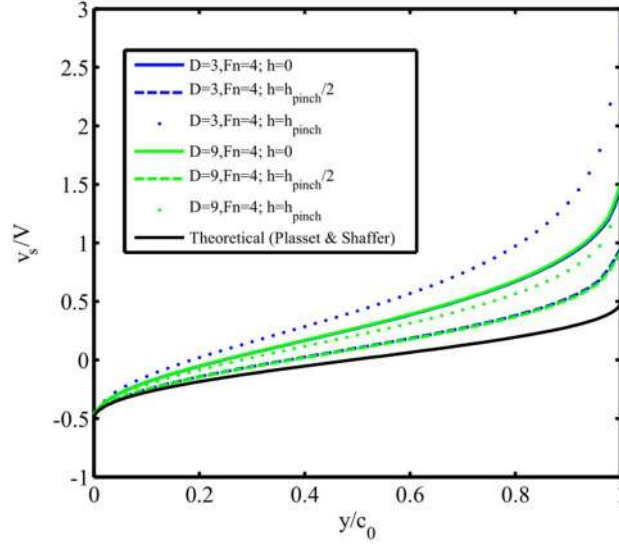
Fig. 28. Variation of the tangential velocity along the wetted body surface of the wedge. $D = M/0.5\rho\pi c_0^2$ is the mass ratio. $Fn = V_0/\sqrt{gc_0}$ is the Froude number. h_{pinch} is the submerged depth at pinch-off. The blue and green lines indicate the numerical solutions of the fully nonlinearly model.

Fig. 29 illustrates the typical evolution of the velocity-drag coefficient of cones vertically entering the water surface, which is similar to that of wedges. The evolution of C_v of the cone goes to the second stage more quickly compared to the wedge. During this stage, C_v is very close to the theoretical value for the relatively large deadrise angle.
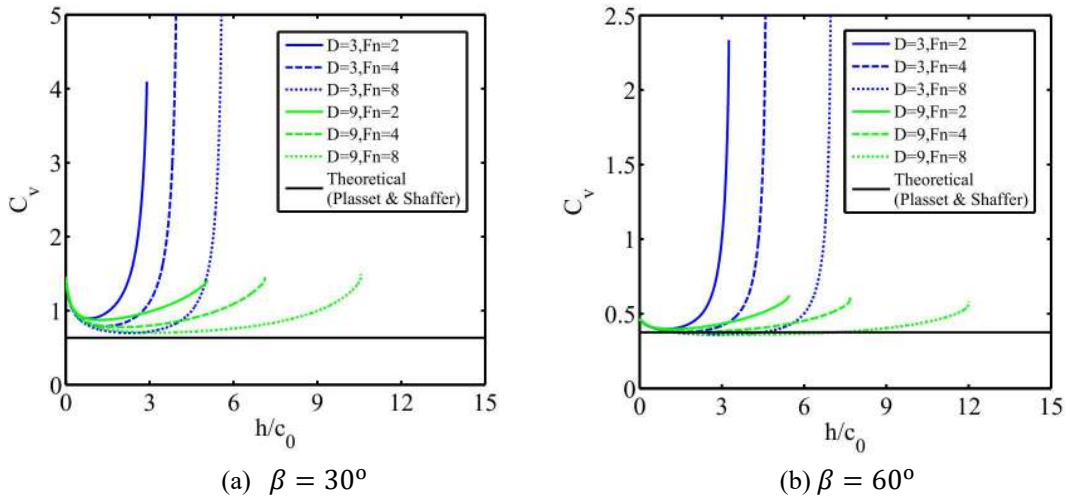

(a) $\beta = 30^o$ (b) $\beta = 60^o$

Fig. 29. Evolution of the velocity-drag coefficient of the cone with the deadrise angle of β vertically entering the water surface until the cavity pinch-off. $D = M/(4\rho c_0^3/3)$ is the mass ratio. $Fn = V_0/\sqrt{gc_0}$ is the Froude number. The blue and green lines indicate the numerical solutions of the fully nonlinearly model.

For the water entry of spheres, the flow separation point is unnecessarily fixed and its position may move along the body surface. May & Woodhull' experiments showed that the corresponding flow separation angle, for the steel spheres, at large Froude numbers ($21 < V_0/\sqrt{gR} < 180$), is about 65°.[35]

The experiments by Aristoff *et al.*[32] showed: the flow separation angle, for the steel spheres, at the Froude numbers $1 < V_0/\sqrt{gR} < 10$, is about 70° before the pinch-off; the flow separation angle, for the spheres made of polypropylene or nylon (corresponding to relatively small mass ratios), is also about 70° at the early stage but can become larger than 90° close to the pinch-off. Here, we only discuss the evolution of the velocity-drag coefficient of steel spheres, of which the flow separation angle can be regarded to be constant. The mass ratio of steel spheres, $M/(\rho\pi R^3/3)$, is as large as about 31. Further, the flow separation angle of 65° or larger make the steel sphere behave like the cone with a relatively large deadrise angle. Based on the previous study, we expect the following: C_v decays quickly at the early stage and it goes to the second after the submerged depth is larger than a few characteristic lengths ; C_v is very close to the limiting value of 0.30-0.31[34] at the second stage; the duration of the second stage is longer for the higher Froude number; the contraction of the air cavity results in the growth of C_v. These are confirmed by the numerical solutions of the fully nonlinear model presented in Fig. 30.
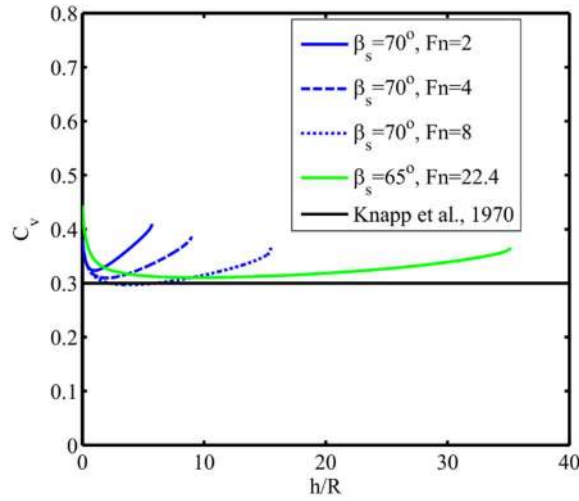

Fig. 30. Evolution of the velocity-drag coefficient of the steel sphere vertically entering the water surface until the cavity pinch-off. $Fn = V_0/\sqrt{gc_0}$ is the Froude number; β_s is the flow separation angle; R is the sphere radius; $C_v = F_z^{(v)}/(0.5\rho V^2\pi R^2)$.

IV. CONCLUSIONS

This work investigated the unsteady hydrodynamic force of solid objects vertically entering water with an air cavity behind the falling body within the framework of potential flow. The unsteady hydrodynamic force is exactly decomposed into three components, i.e. the acceleration term $F_z^{(a)}$, the gravity term $F_z^{(g)}$ and the velocity term $F_z^{(v)}$. The acceleration term is equal to the high-frequency added mass times the body acceleration, i.e. $F_z^{(a)} = -A_{33}\dot{V}$. The gravity term consists of a hydrostatic term and a dynamic term. The hydrostatic term is obtained by integrating the term, $-\rho gz$, in the Bernoulli's equation over the wetted body surface, is upwards, and strongly overestimates $F_z^{(g)}$. The dynamic term is downwards. The added mass and the gravity term can be well estimated by the proposed simplified models, which assume a uniform cavity behind the falling body. Near the undisturbed free surface, the added mass grows strongly with increasing the submerged depth. It tends to be steady after the submerged depth is greater than a few characteristic lengths (the characteristic length, c_0, is defined as half of the wetted breadth). The solution of the added mass of different geometries, at the still water surface and deeply submerged, is presented. The added mass can be approximated as $A_{33} = \pi\rho c_0^2/2$ for the circular cylinder and the wedge with small deadrise angles, $A_{33} = 4\rho c_0^3/3$ for the cone with small

deadrise angles, and $A_{33} = \pi \rho c_0^3/3$ for spheres. The key physical parameters of affecting the gravity term are the projected wetted area, the submerged depth and the body geometry. The gravity term is proportional to the projected wetted area. Excluding the buoyance, i.e. the weight of the water with the volume of the wetted body, the gravity term is not sensitive to the body geometry at small submerged depth, but it is strongly influenced by the body geometry at large submerged depth. The analytical solution of $F_z^{(g)}$ of the wedge with any deadrise angle is presented. Asymptotically ($h \to \infty$), $F_z^{(g)}$ is proportional to the square root of the submerged depth. For the three-dimensional bodies, the dimensionless gravity term follows $\bar{F}_g^{(z)} = \alpha \bar{h}^\gamma$, where $\bar{h} = h/c_0$ and γ is about 0.83. The velocity term is represented as the drag coefficient, $C_v = F_z^{(v)}/(0.5\rho V^2 S)$, which is characterized by the body geometry. The submerged depth and the cavity shape influence the drag coefficient through modifying the velocity field near the wetted body. The evolution of the drag coefficient can be divided into three stages: i) near the still water surface, C_v decays strongly with increasing the submerged depth; ii) after the submerged depth is greater than a few characteristic lengths, C_v evolves gently and is reasonably constant; and (iii) C_v grows due to the contraction of the air cavity. C_v at the second stage becomes closer to the limiting value, which corresponds to the steady cavity flow at zero cavitation number. Larger mass ratios and/or higher Froude numbers result in the longer period of the second stage. Smaller mass ratios can lead to the dramatical growth of C_v close to the pinch-off of the open cavity.

ACKNOWLEDGEMENTS

REFERENCES

1. T. Von Kármàn, 1929. The impact on seaplane floats during landing. National Advisory Committee for Aeronautics. Technical note No. 321.
2. O.M. Faltinsen, 1990. Sea loads on ships and offshore structures. Cambridge University Press.
3. O.M. Faltinsen, 2005. Hydrodynamics of high-speed marine vehicles. Cambridge University Press.
4. A. May, "Vertical entry of missiles into water," J. Appl. Phys. **23**,1362–1372 (1952).
5. A. May, 1975. Water entry and the cavity-running behavior of missiles. Tech. Rep. 20910, Nav. Surf. Weapons Cent., White Oak Lab., MD.
6. T. T. Truscott, 2009. Cavity dynamics of water entry for spheres and ballistic projectiles. PhD diss. Mass. Inst. Technol., Cambridge, MA.
7. T. T. Truscott, B. P. Epps and J. Belden, "Water entry of projectiles," Annu. Rev. Fluid Mech. **46**, 355–378 (2014).
8. D. H. Peregrine, "Water wave impact on walls," Annu. Rev. Fluid Mech. **35**, 23-43 (2003).
9. C. Lugni, A. Bardazzi, O.M. Faltinsen, G. Graziani, "Hydroelastic slamming response in the evolution of a flip-through event during shallow-liquid sloshing," Phys. Fluids **26**, 032108 (2014).
10. J. W. Glasheen and T. A. McMahon, "A hydrodynamic model of locomotion in the Basilisk lizard," Nature **380**, 340-342 (1996).
11. J. W. Glasheen and T. A. McMahon, "Vertical water entry of disks at low Froude numbers," Phys. Fluids **8**, 2078–2083 (1996).

12. H. Wagner, "Über Stoß- und Gleitvorgänge an der Oberfläche von Flüssigkeiten", Z. Angew. Math. Mech. **12**, 193–215(1932).

13. Z. N. Dobrovol'skaya, "On some problems of similarity flow of fluid with a free surface," J. Fluid Mech. **36**, 805–829 (1969).

14. R. Cointe and J.-L. Armand, "Hydrodynamic impact analysis of a cylinder", ASME J. Offshore Mech. Arc. Eng. **109**, 237–243 (1987).

15. A. A. Korobkin and V. V. Pukhnachov, "Initial stage of water impact," Annu. Rev. Fluid Mech. **20**,159–85(1988).

16. R. Cointe, 1991. Free surface flows close to a surface-piercing body. Mathematical Approaches in Hydrodynamics, SIAM, Philadelphia, USA, 319–334.

17. S. D. Howison, J. R. Ockendon and S.K. Wilson, "Incompressible water entry problems at small deadrise angles", J. Fluid Mech. **222**, 215–230 (1991).

18. R. Zhao and O. M. Faltinsen, "Water entry of two-dimensional bodies". J. Fluid Mech. **246**, 593–612 (1993).

19. O. M. Faltinsen, R. Zhao, 1998. Water entry of ship sections and axisymmetric bodies, AGARD Report 827, High Speed Body Motion in Water.

20. Y. -M. Scolan and A. A. Korobkin, "Three-dimensional theory of water impact. Part 1. Inverse Wagner problem," J. Fluid Mech. **440**, 293–326 (2001).

21. O. M. Faltinsen, "Water entry of a wedge with finite deadrise angle," J. Ship Res. **46**, 39–51 (2002).

22. A.A. Korobkin, "Analytical models of water impact," Eur. J. Appl. Math. **15**, 821–838 (2004).

23. J. Wang and O. M. Faltinsen, "Improved numerical solution of Dobrovol'skaya's boundary integral equations on similarity flow for uniform symmetrical entry of wedges," Appl. Ocean Res. **66**, 23–31(2017).

24. J. Wang, C. Lugni and O. M. Faltinsen, "Analysis of loads, motions and cavity dynamics during freefall wedges vertically entering the water surface", Appl. Ocean Res. **51**, 38–53 (2015).

25. V. Duclaux, F. Caillé, C. Duez, C. Ybert, L. Bocquet and C. Clanet, "Dynamics of transient cavities," J. Fluid Mech. **591**,1–19 (2007).

26. A. M. Worthington and R. S. Cole, "Impact with a liquid surface studied by the aid of instantaneous photography. Paper II," Phil. Trans. R. Soc. Lond. A **194**, 175–199 (1900).

27. D. Gilbarg and R. A. Anderson, "Influence of atmospheric pressure on the phenomena accompanying the entry of spheres into water," J. Appl. Phys. **19**,127–139 (1948).

28. M. Lee, R. G. Longoria and D. E. Wilson, "Cavity dynamics in high-speed water entry," Phys. Fluids **9**, 540–550 (1997).

29. S. Gaudet, "Numerical simulation of circular disks entering the free surface of a fluid," Phys. Fluids **10**, 2489-2499 (1998).

30. R. Bergmann, D. van der Meer, S. Gekle, A. van der Bos and D. Lohse, "Controlled impact of a disk on a water surface: cavity dynamics," J. Fluid Mech. **633**, 381–409 (2009).

31. H. Yan, Y. Liu, J. Kominiarczuk and D. K. P. Yue, "Cavity dynamics in water entry at low Froude numbers," J. Fluid Mech. **641**, 441–461 (2009).

32. J. M. Aristoff, T. T. Truscott, A. H. Techet and W. M. Bush, "The water entry of decelerating spheres," Phys. Fluids **22**, 032102 (2010).

33. M.S. Plesset and P. A. Shaffer, "Cavity drag in two and three dimensions," J. Appl. Phys. **19**, 934-939 (1948).

34. R. T. Knapp, J.W. Daily, F.G. Hammitt, 1970. Cavitation. New York: McGraw-Hill.

35. A. May and J. C. Woodhull, "Drag coefficients of steel spheres entering water vertically," J. Appl. Phys. **19**, 1109-1121 (1948).

36. I. R. Peters, S. Gekle and D. Lohse, 'Air Flow in a collapsing cavity', Phys. Fluids **25**, 032104 (2013).

37. J. Wang, C. Lugni and O.M. Faltinsen, "Experimental and numerical investigation of a freefall wedge vertically entering the water surface", Appl. Ocean Res. **51,** 181–203 (2015).

38. C. Lugni, 1995.A study of the fluid dynamic field around a floating structure. Master thesis, University of Rome, La Sapienza.

39. D. G. Dommermuth and D. K. P. Yue. "Numerical simulations of nonlinear axisymmetric flows with a free surface," J. Fluid Mech. **178**, 195–219 (1987).

40. J. Wang and O.M. Faltinsen, "Numerical investigation for air cavity formation during the high-speed water entry of wedges," J. Offshore Mech. Arct. Eng. **135**, n1(2013).